Available online at www.sciencedirect.com

ScienceDirect
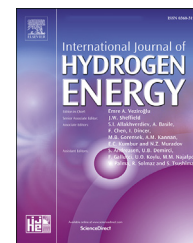
Fault-tolerant control through dynamic surface triple-step approach for proton exchange membrane fuel cell air supply systems

Yulei Wang [a,b], Meng Li [a], Jinwu Gao [c], Hongqing Chu [b], Hong Chen [a,b,*]

[a] Department of Control Science and Engineering, Tongji University, Shanghai, 200092, China
[b] Clean Energy Automotive Engineering Center, Tongji University, Shanghai, 201804, China
[c] State Key Laboratory of Automotive Simulation and Control, Jilin University, Changchun, 130022, China

HIGHLIGHTS

- The air supply system for proton exchange membrane fuel cells (PEMFCs) is modeled.
- Valve stuck and supply manifold leakage faulty cases are considered.
- A fault-tolerant control (FTC) scheme is proposed by a triple-step approach.
- The stability of the overall system is proved using Lyapunov method.
- A high-fidelity PEMFC model is applied to confirm the proposed FTC method.

ARTICLE INFO

ABSTRACT

Due to complex electrochemical and thermal phenomena, varying operations towards automotive applications, and vulnerable ancillaries in proton exchange membrane fuel cells (PEMFCs), fault diagnosis and fault-tolerant control (FTC) design have become important aspects to improve the reliability, safety and performance of PEMFC systems. This paper presents a novel FTC scheme for automotive PEMFC air supply systems via coordinated control of the air flow rate and the pressure in cathodes. A dynamic surface triple-step approach is first proposed considering nonlinear dynamics and the multi-input multi-output (MIMO) property, which combines the advantage of dynamic surface control in avoiding an "explosion of complexity" and the advantage of triple-step control in guaranteeing a simple structure and high performance. The normal case, the faulty case at the supply manifold and the faulty case in the back pressure valve are considered in the FTC design, with the stability of the overall system proved using Lyapunov methods. MATLAB/Simulink simulations with a high-fidelity PEMFC model verify the effectiveness of the proposed FTC scheme in regulating the air flow rate and oxygen excess ratio and maintaining the pressure of the cathode at a desired level even under faulty conditions.

* Corresponding author. Department of Control Science and Engineering, Tongji University, Shanghai, 200092, China.
E-mail address: chenhong2019@tongji.edu.cn (H. Chen).

Introduction

Fuel cells produce clean energy from chemical reactions between anodes and cathodes and thus are widely regarded as potential alternative energy conversion technologies in the framework of the Paris Climate Agreement [1]. Among various types of fuel cells, proton exchange membrane fuel cells (PEMFCs) are the most promising for automotive applications due to their low-temperature operation, high efficiency and favorable power density [2–4]. A typical PEMFC system requires an air supply subsystem at the cathode to manipulate the compressor motor and valve, providing a sufficient reactant flow (with a desired excess ratio) to minimize auxiliary power consumption and maintain the pressure equilibrium between the cathode and the anode in order to prolong the service life of PEMFCs [5–7].

One of the most challenging tasks in the PEMFC air supply system is coordinated control of the air flow rate and the pressure in the cathode [5,8,9]. Because the inlet and outlet flow rates of the cathode are mutually influenced, there exists a mutual coupling between the air flow rate into the cathode and the pressure of the cathode. In general, a high air flow rate increases the reaction kinetics of electrochemical reactions, resulting in a high power density and great stack efficiency but a low net available power from the PEMFC system because of the requirement of high parasitic power [10]. In contrast, a low air flow rate is prone to oxygen starvation, which may damage the polymer electrolyte membrane due to inadequate electrochemical reactions [3]. Furthermore, a high cathode pressure can not only effectively improve the catalytic rate but also increase the difficulty of tracking current and power variations of the PEMFC system because of varying load demands, especially in automotive applications [11]. Instead, a low cathode pressure in the cathode may cause hydrogen starvation, which can likely damage the fuel cell membrane and catalyst layer [12]. In conclusion, PEMFCs are nonlinear, multi-input multi-output (MIMO) and strongly coupled dynamic systems, and thus, the design of model-based nonlinear control strategies is always welcome.

To regulate the air flow rate and pressure, many advanced nonlinear control strategies have been implemented in PEMFC air supply systems. In Refs. [5,9,13–15], the nonlinear control concept of exact input-output linearization with extended proportion-integral-derivative (PID) control structures was applied for PEMFCs with feedback linearization and differential flatness techniques. To improve the transient control performance and robustness against model uncertainties and disturbances, varied sliding mode control (SMC) schemes were developed by Refs. [16–18,20,42] to regulate the air flow rate and the cathode pressure simultaneously. The experimental tests were satisfactory, but chattering effects could not be prevented, possibly causing the closed-loop control system to be sensitive to measurement noise and high energy consumption to be harmful to actuator reliability. Instead, nonlinear model predictive control (MPC) approaches were proposed to optimize the air flow in real time and ensure adequate oxygen supply under constraint satisfaction [21–23]. The main disadvantage of using nonlinear MPC is the requirement of online optimization, which is normally difficult for real applications because of the high computational burden. Recently, a modularized nonlinear control law consisting of three control parts was proposed for PEMFCs based on triple-step control (TSC) [24,25]. The TSC design is amenable for industrial engineers to understand sophisticated nonlinear control algorithms. Nevertheless, these aforementioned results mainly focus on PEMFC air supply systems without back pressure valve control, and thus cannot deal with the coupled dynamics of the air flow and pressure of the cathode. In addition, the existing TSC design suffers from the widely recognized "explosion of complexity" problem arising from high-order derivations of control outputs. Hence, the first motivation of the present paper is to develop a modified TSC method with the aid of dynamic surface control [26,27] and apply it to PEMFC air supply systems.

Fault diagnosis and fault-tolerant control (FTC) are other significant issues associated with PEMFCs for regarding durability, reliability and safety. The PEMFC is a particularly complex system with various types of auxiliary components, sensors and actuators, thus increasing the probability of a fault occurrence. Therefore, adding fault tolerance mechanisms into the air supply system allows maintaining stability and acceptable performance despite potential faults. In Ref. [28], an active FTC system was proposed for a fuel cell/battery hybrid powertrain applied to a city bus. Four algorithms were proposed to detect and isolate sensor faults, and then, two soft sensors were constructed for the control module. For water management of the PEMFC, an analytical residual-based diagnosis scheme was built by Ref. [29] for the output voltage of the fuel cell and the pressure of the cathode using an artificial neural network (ANN). Then, a reconfiguration mechanism and an adjustable controller were constructed to update the setpoint of the oxygen excess ratio to avoid flooding faults in the PEMFC. Considering both flooding and membrane drying faults, Wu and Zhou [30] proposed an analytical model-based fault detection and isolation (FDI) method and built three nonlinear controllers based on feedback linearization, which switched to regulate both the PEMFC voltage and pressure difference for normal and faulty cases. Furthermore, Polverino et al. [31] proposed guidelines for the design of a model-based diagnostic algorithm for PEMFCs, where structural analysis and causal computation were used to design the minimal group of residual generators. Nine faults on the stack, auxiliaries and sensors were independently analyzed in the simulation environment. For actuator faults such as the loss of effectiveness or locking in place, a fault-tolerant strategy was presented by Ref. [32] for a bioethanol processor system integrated into a PEMFC based on a hierarchical control scheme, in which a control allocation module was designed for online redistribution of virtual commands from faulty actuators to healthy actuators. Recently, Yan et al. [33] developed a model-based sensor fault diagnosis method based on structural analysis. An active FTC framework was then proposed based on the smooth-switching SMC algorithm. The experimental results demonstrated the effectiveness of the proposed FDI/FTC strategy. In Ref. [34], fault diagnosis in the air supply system was presented based on an augmented linear parameter-varying (LPV) observer, and an active FTC was developed to regulate oxygen stoichiometry. Two common faults in the system

components were studied: a supply manifold fault (pipeline gas leakage or blockage) and a back pressure valve fault. Nevertheless, there exists no literature on investigating an integrated design of FDI within FTC [35] since uncertainties of modeling and fault estimation may affect the quality and robustness of the FTC system. Therefore, the second motivation of the present article is to revisit the FTC issue [34] with the overall stability of fault estimation, fault accommodation and control reconfiguration.

According to the literature, controlling a PEMFC air supply system not only considers its MIMO and nonlinear model but also needs to maintain the overall stability and acceptable performance in case of component failures, which has a significant influence on PEMFC safety and reliability in practice. Note that the triple-step approaches [24,25] are preliminarily used to regulate the air flow rate for the desired oxygen excess ratio. However, issues regarding coordinated control of the air flow rate and pressure, dynamic surface control and/or integrated FDI/FTC against failures and faults have seldom been investigated.

As shown in Fig. 1a, the state-of-the-art approach for PEMFCs uses a cascaded framework through a combination of dynamic surface control and TSC. The challenge for PEMFCs comes from three different aspects shown in Fig. 1b: model nonlinearity, coordinated control of the air flow rate and pressure in the cathode, and potential leakage and stuck faults. As shown in Fig. 1c, the key to regulating PEMFCs under faults is to construct the active FTC scheme, which is able to accommodate the component faults automatically by maintaining the overall system stability and acceptable performance. The main contributions are as follows:

1. In contrast to Refs. [5,8,9], a coordinated control scheme that regulates the air flow rate and pressure of the cathode simultaneously is proposed to offer high-quality control with increased efficiency and safety.
2. Unlike purely using TSC [24,25], the TSC presented here is used for MIMO systems and adds dynamic surface techniques [26] to avoid the "explosion of complexity" problem.
3. Different from Ref. [34], both supply manifold faults and back pressure valve faults are considered from the viewpoint of integrated FDI/FTC, with the stability of the overall system proved via Lyapunov methods.

The rest of the paper is organized as follows. First, three control-oriented models are established to describe the normal and faulty conditions of the PEMFC air supply system. Next, the problem statement is given. Second, elegant FTC strategies are proposed for the PEMFC system against different component faults. The following section shows simulation results, which demonstrate the effectiveness of the proposed FTC scheme. Finally, the conclusion is presented.

System modeling and problem statement

In this section, the PEMFC air supply system with faults is investigated. Nonlinear equations are derived by manifold filling dynamics and experimental MAP functions. Then, control-oriented models for normal and faulty cases are obtained as three groups of nonlinear equations.

Modeling and analysis of PEMFC air supply systems

The proposed model is based on the work of Pukrushpan et al. [12], including a further analysis of a supply manifold fault (pipeline gas leakage or blockage) and a back pressure valve fault (valve locking in place). The considered system is an air supply cathode PEMFC oriented to automotive applications, and from a control viewpoint, it is simplified to include a centrifugal air compressor, an air supply manifold, a cathode, a throttle and several essential sensors to measure speed, temperature, current, air flow rate and pressure. A schematic diagram of the PEMFC air supply system is presented in Fig. 2, where the analyzed faults are labeled by triangles.

The procedure of the air supply system is as follows: At the cathode side, the air compressor feeds the PEMFC with oxygen taken from the surroundings under ambient conditions, with a given pressure and temperature. The supply manifold connects the air compressor to the cathode inlet, between which the intercooler and humidifier units provide the required temperature and humidity, respectively, to ensure the correct operation of the stack. After air enters the cathode for electrochemical reactions, the air passes through the water-air separation device and throttle for drying and exhausting,
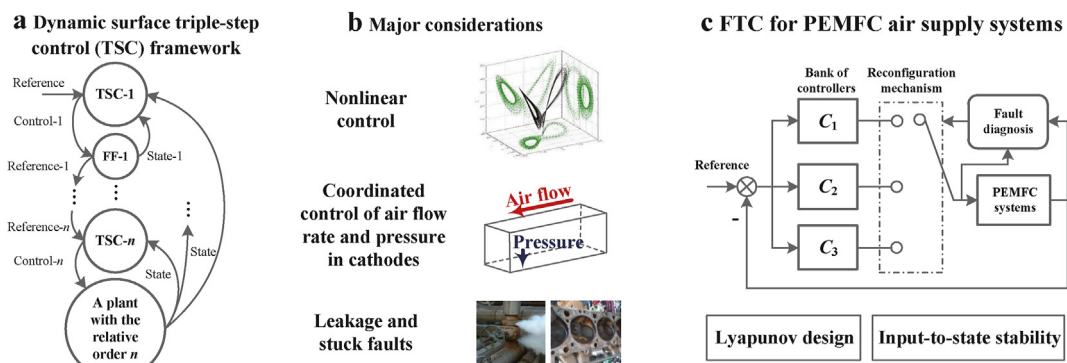

Fig. 1 – Dynamic surface triple-step FTC scheme of PEMFC systems. a Dynamic surface triple-step framework. b Major considerations for PEMFCs include nonlinear control, coordinated control of the air flow rate and pressure in the cathode, and leakage and stuck faults. c FTC scheme for the PEMFC system with a Lyapunov design and input-to-state stability.
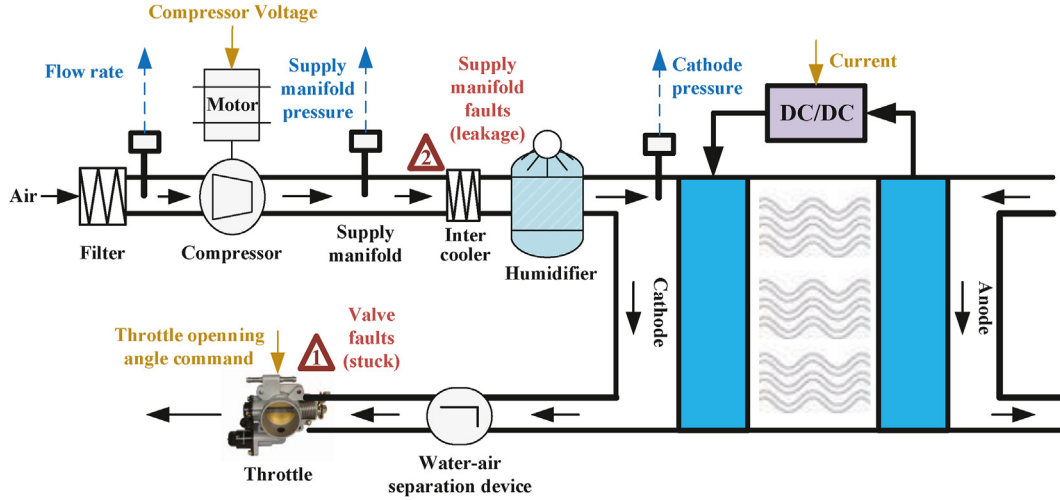
Fig. 2 — Schematic diagram of the PEMFC air supply system.

respectively. Note that the compressor supply voltage and throttle opening commands are used as manipulation variables to regulate the inlet air flow rate and pressure in the cathode. The speed sensor at the compressor, the pressure sensor at the supply manifold inlet, the flow and pressure sensors at the cathode inlet and the angle opening sensor at the throttle are used for state-feedback control. The load current is measured and viewed as a known disturbance to determine the desired air flow rate and pressure of the cathode, to maintain the available oxygen excess ratio.

The compressor model is separated into a static compressor map to describe the air flow rate through the compressor and the dynamics of the compressor and motor speed. Note that the compressor outlet flow rate is positive relative to the compressor speed and negative relative to the compression ratio. Then, the dynamical equations for the compressor model are given as [12].

$$\dot{\omega}_{cp} = \frac{1}{J_{cp}}\left(\tau_{cm} - \tau_{cp}\right), \tag{1a}$$

$$\tau_{cm} = \eta_{cm}\frac{k_t}{R_{cm}}\left(v_{cm} - k_v\omega_{cp}\right), \tag{1b}$$

$$\tau_{cp} = \frac{C_p}{\omega_{cp}}\frac{T_{at}}{\eta_{cp}}\left[\left(\frac{p_{sm}}{p_{at}}\right)^{\frac{\gamma-1}{\gamma}} - 1\right]W_{cp}, \tag{1c}$$

where J_{cp} is the inertia of the compressor, ω_{cp} is the angular velocity of rotation with the compressor speed $N_{cp} = \frac{30}{\pi}\omega_{cp}$, τ_{cm} is the compressor torque input, τ_{cp} is the torque required to drive the compressor, v_{cm} is the compressor voltage, p_{sm} is the pressure of the air supply manifold, p_{at} is the atmospheric pressure, T_{at} is the atmospheric temperature, C_p is specific heat capacity, γ is the ratio of specific heat, η_{cp} is maximum compression efficiency and η_{cm}, k_t, R_{cm}, and k_v are mechanical parameters of
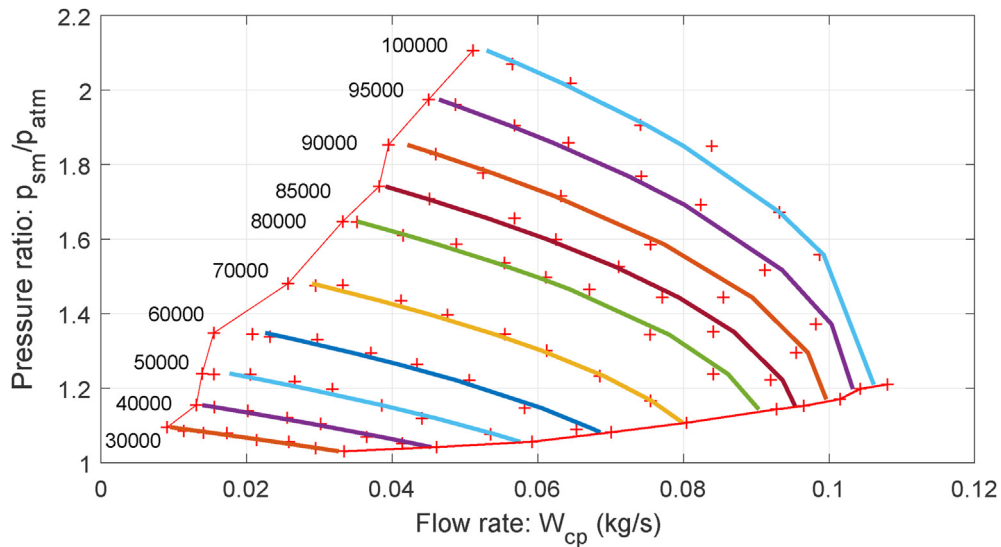

Fig. 3 — Comparison of the experimental data and fitting results with the following coefficients: $p_0 = 0.1928$, $p_1 = -9.23 \times 10^{-6}$, $p_2 = 6.63 \times 10^{-6}$, $p_3 = 0.3058$, $p_4 = 7.24 \times 10^{-11}$, $p_5 = -0.501$, $p_6 = -7.89 \times 10^{-11}$ and $p_7 = 4.29 \times 10^{-6}$.

the compressor. The flow rate W_{cp} related to the compressor speed N_{cp} and the pressure ratio $\frac{p_{sm}}{p_{at}}$ is calibrated from experimental data. As shown in Fig. 3, the function can be approximated by the following second-order polynomial function:

$$W_{cp} = p_0 + p_1 N_{cp} + p_2 N_{cp}\frac{p_{sm}}{p_{at}} + p_3\frac{p_{sm}}{p_{at}} + p_4 N_{cp}^2 + p_5\left(\frac{p_{sm}}{p_{at}}\right)^2$$
$$+ p_6 N_{cp}^2\frac{p_{sm}}{p_{at}} + p_7 N_{cp}\left(\frac{p_{sm}}{p_{at}}\right)^2, \tag{2}$$

where p_i, $i = 0, ..., 7$ are the corresponding fitting coefficients.

The air supply manifold connects the compressor and the cathode. Based on the ideal gas law and the assumption of constant temperature in the manifold, the dynamics of the air pressure p_{sm} inside the air supply manifold can be modeled as

$$\dot{p}_{sm} = \frac{T_{cp}R_a}{V_{sm}}(W_{cp} - W_{sm}), \tag{3}$$

where R_a is the gas constant of air and V_{sm} is the manifold volume. The temperature of air leaving the compressor T_{cp} is given as [36]. [][][].

$$T_{cp} = T_{at}\left[1 + \frac{1}{\eta_{cp}}\left(\left(\frac{p_{sm}}{p_{at}}\right)^{\frac{\gamma-1}{\gamma}} - 1\right)\right], \tag{4}$$

and the outlet flow rate at the supply manifold W_{sm} can be approximated in a linear nozzle flow model [20]:

$$W_{sm} = k_{sm}(p_{sm} - p_{ca}), \tag{5}$$

where k_{sm} is the flow constant and p_{ca} is the pressure of the cathode.

The dynamics of the cathode are used to describe transient changes in the air mass and pressure. Given that the inlet and outlet temperatures of the cathode are constant and the same, using the ideal gas and electrochemical equations, the balance of the dynamic pressure is described as [12].

$$\dot{p}_{ca} = \frac{R_a T_{st}}{V_{ca}}(W_{ca,in} - W_{ca,out}) - \frac{R_{O_2}T_{st}}{V_{ca}}W_{O_2,react}, \tag{6}$$

where $W_{ca,in}$ is the inlet flow rate of the cathode and V_{ca} and R_{O_2} are the cathode volume and the oxygen gas constant, respectively. T_{st} is the temperature within the cathode. The oxygen consumption rate $W_{O_2,react}$ can be calculated with respect to the load current I_{st} [37]:

$$W_{O_2,react} = \frac{n_{cell}M_{O_2}}{4F}I_{st}, \tag{7}$$

where n_{cell} is the number of cells in series, M_{O_2} is the oxygen molar mass, and F is the Faraday constant. The outlet air flow rate $W_{ca,out}$ is given by Ref. [38].

$$W_{ca,out} = \sin^2\left(\frac{\pi}{180}\theta\right)\frac{C_{D,tr}A_{T,tr}p_{ca}}{\sqrt{RT_{st}}} \times \left(\frac{1}{\gamma}\right)^{\frac{1}{2}}\left(\frac{2}{\gamma+1}\right)^{\frac{\gamma+1}{2(\gamma-1)}}, \tag{8}$$

where $C_{D,tr}$ is the throttle discharge coefficient, $A_{T,tr}$ is the maximum throttle opening area, $\bar{R}$ is the universal gas constant and θ is the throttle opening angle that can be further adjusted to regulate the outlet flow rate of the cathode.

Control-oriented models for normal and faulty scenarios

Normal scenario

In the normal case, the outlet flow rate of the air supply manifold W_{sm} is approximately equal to the inlet flow rate of the cathode $W_{ca,in}$, i.e.,

$$W_{sm} = W_{ca,in}, \tag{9}$$

and the closed-loop throttle control can be modeled as a first-order model:

$$\dot{\theta} = \frac{1}{T_s}(-\theta + \theta^*), \tag{10}$$

where T_s is the response time constant of the throttle and θ^* is the command of the throttle opening angle.

By combining (1)–(10), the control-oriented model for the normal case can be derived as

$$\dot{x}_1 = -a_1 x_1 - \frac{a_2}{x_1}\left(\left(\frac{x_2}{a_3}\right)^{a_4} - 1\right) \times h_1(x_1, x_2) + a_5 u_1, \tag{11a}$$

$$\dot{x}_2 = a_6\left[1 + a_7\left(\left(\frac{x_2}{a_3}\right)^{a_4} - 1\right)\right] \times [h_1(x_1, x_2) - a_8(x_2 - x_3)], \tag{11b}$$

$$\dot{x}_3 = a_9(x_2 - x_3) - a_{10}d - a_{11}h_2(x_3, x_4), \tag{11c}$$

$$\dot{x}_4 = \frac{1}{a_{12}}(-x_4 + u_2), \tag{11d}$$

where $x_1 = \omega_{cp}$, $x_2 = p_{sm}$, $x_3 = p_{ca}$ and $x_4 = \theta$ are the system states, $u_1 = \tau_{cm}$ and $u_2 = \theta^*$ are the control inputs, $d = I_{st}$ is the known disturbance, $h_1 = W_{cp}$ and $h_2 = x_3\sin^2\left(\frac{\pi}{180}x_4\right)$ are the nonlinear functions, and the lumped parameters in (11) are given as

$$a_1 = \frac{\eta_{cm}k_t k_v}{J_{cp}R_{cm}}, \; a_2 = \frac{C_p T_{at}}{J_{cp}\eta_{cp}}, a_3 = p_{at}, \; a_4 = \frac{\gamma-1}{\gamma}, \; a_5 = \frac{\eta_{cm}k_t}{J_{cp}R_{cm}},$$
$$a_6 = \frac{R_a T_{at}}{V_{sm}} a_7 = \frac{1}{\eta_{cp}}, \; a_8 = k_{sm}, \; a_9 = \frac{R_a T_{st}}{V_{ca}}k_{sm}, \; a_{10}$$
$$= \frac{R_{O_2}M_{O_2}T_{st}n_{cell}}{4V_{ca}F} a_{11} = \frac{R_a T_{st}}{V_{ca}}\frac{C_{D,tr}A_{T,tr}}{\sqrt{RT_{st}}}(\gamma)^{\frac{1}{2}}\left(\frac{2}{\gamma+1}\right)^{\frac{\gamma+1}{2(\gamma-1)}}, \; a_{12} = T_s.$$

To regulate the air flow rate and pressure of the cathode, the control outputs $y_1 = W_{ca,in}$ and $y_2 = p_{ca}$ are presented as

$$y_1 = a_8(x_2 - x_3), \tag{12a}$$

$$y_2 = x_3, \tag{12b}$$

which indicates that the control problem in the normal case is nonlinear and MIMO.

Back pressure valve faulty scenario

The second scenario is under a back pressure valve fault that represents a stuck malfunction of the throttle located at the cathode outlet and disables the control freedom of the throttle,

which implies that outputs y_1 and y_2 cannot be regulated by throttle commands u_2. Consequently, with the dynamics described in (1)-(10) by replacing the stuck angle as a fault $f_1 = \theta$, the control-oriented model for the faulty scenario is given as

$$\dot{x}_1 = -a_1 x_1 - \frac{a_2}{x_1}\left(\left(\frac{x_2}{a_3}\right)^{a_4} - 1\right) \times h_1(x_1, x_2) + a_5 u_1, \quad (13a)$$

$$\dot{x}_2 = a_6\left[1 + a_7\left(\left(\frac{x_2}{a_3}\right)^{a_4} - 1\right)\right] \times [h_1(x_1, x_2) - a_8(x_2 - x_3)], \quad (13b)$$

$$\dot{x}_3 = a_9(x_2 - x_3) - a_{10}d - a_{11}h_2(x_3, f_1), \quad (13c)$$

where $h_2(x_3, f_1) = x_3 \sin^2\left(\frac{\pi}{180} f_1\right)$. Then, the system under the stuck fault only governs the first control output:

$$y_1 = W_{ca,in} = a_8(x_2 - x_3), \quad (14a)$$

and thus, FTC becomes a single-input single-output (SISO) control problem.

Supply manifold faulty scenario

The third scenario concerns a supply manifold fault involving a gas leak at the supply manifold outlet, which may be related to sealing degradation of the cathode inlet nozzle valve or to a pipe crack. To model this case, the relationship between the outlet flow rate of the supply manifold W_{sm} and the inlet flow rate of the cathode $W_{ca,in}$ is modified by adding a leakage fault f_2 [34]:

$$W_{sm} = W_{ca,in} + f_2. \quad (15)$$

Then, the control-oriented model for the leakage faulty scenario is described as

$$\dot{x}_1 = -a_1 x_1 - \frac{a_2}{x_1}\left(\left(\frac{x_2}{a_3}\right)^{a_4} - 1\right) \times h_1(x_1, x_2) + a_5 u_1, \quad (16a)$$

$$\dot{x}_2 = a_6\left[1 + a_7\left(\left(\frac{x_2}{a_3}\right)^{a_4} - 1\right)\right] \times [h_1(x_1, x_2) - a_8(x_2 - x_3)], \quad (16b)$$

$$\dot{x}_3 = a_9(x_2 - x_3) - a_{13}f_2 - a_{10}d - a_{11}h_2(x_3, x_4), \quad (16c)$$

$$\dot{x}_4 = \frac{1}{a_{12}}(-x_4 + u_2), \quad (16d)$$

where $a_{13} = \frac{R_a T_{st}}{V_{ca}}$. The control outputs under the leakage fault are rewritten as

$$y_1 = W_{ca,in} = W_{sm} - f_2 = a_8(x_2 - x_3) - f_2, \quad (17a)$$

$$y_2 = x_3. \quad (17b)$$

Note that the presented faults are only two special cases among numerous faults that can occur in automotive PEMFCs. The choice is made and driven by the need to construct the corresponding control-oriented models and investigate the capability of FTC algorithms in the next section.

Control problem statement

Note that one of the key variables affecting the PEMFC performance is the oxygen excess ratio λ_{O_2}, defined as [24].

$$\lambda_{O_2} = \frac{4Fx_{O_2}}{n_{cell}}\frac{W_{ca,in}}{I_{st}} = a_{14}\frac{y_1}{I_{st}}, \quad (18)$$

where x_{O_2} is the oxygen mass fraction in air. Referring to Ref. [39], a suitable oxygen excess ratio can be calculated as a function of the load current:

$$\lambda_{O_2}^*(I_{st}) = 5 \times 10^{-8}I_{st}^3 - 2.87 \times 10^{-5}I_{st}^2 + 2.23 \times 10^{-3}I_{st} + 2.5. \quad (19)$$

Substituting (19) into (18) generates the reference of the flow rate y_1 as

$$y_1^* = \frac{I_{st}}{a_{14}}\lambda_{O_2}^*(I_{st}). \quad (20)$$

Note that pressure control in the cathode maintains a small pressure error between the cathode and the anode [12]. In addition, the output voltage of a PEMFC stack can be affected by cathode pressure, and thus, it is useful for load transients to adjust the pressure value in real time [8]. Based on empirical research, the reference of the cathode pressure y_2 is then calibrated by

$$y_2^* = 1.54 \times 10^{-2}I_{st}^3 - 10.25I_{st}^2 + 2327I_{st} - 28240. \quad (21)$$

According to the control-oriented models (11), (13) and (16), to improve the normal control specification and the FTC ability of PEMFC air supply systems, the control objective of the paper is to design a reconfigurable FTC law $u = [u_1, u_2]^T$ such that the control outputs $y = [y_1, y_2]^T$ are input-to-state stable (ISS) and converge to the sufficiently small neighborhood of the reference $y^* = [y_1^*, y_2^*]^T$ in the presence of the back pressure valve and supply manifold faults $f = [f_1, f_2]^T$.

Fault-tolerant control of PEMFC air supply systems

In this section, a novel FTC design is proposed for solving the air supply control problem of PEMFCs. The design procedure mainly consists of two parts: a dynamic surface triple-step approach to regulate the air flow rate and pressure simultaneously and a reconfigurable controller design of PEMFCs against both stuck and leakage faults.

Dynamic surface triple-step approach

In this subsection, a dynamic surface triple-step controller is designed for the normal air supply system in (11). Different from the original TSC, the proposed approach designs a hierarchical control architecture, of which each layer constructs a first-order triple-step controller, and a first-order filter is used to connect the adjacent layers to overcome the explosion of terms. The final control law can be derived with a step-by-step procedure, and the details for PEMFCs are given as follows.

Layer 1: Define the tracking error for y as

$$S_1 = \begin{bmatrix} s_{11} \\ s_{12} \end{bmatrix} = \begin{bmatrix} y_1 - y_1^* \\ y_2 - y_2^* \end{bmatrix}, \quad (22)$$

and by taking the time derivative of (22) along the dynamics of (11), we have

$$
\dot{S}_1 = \begin{bmatrix} -a_6 a_8 \left[1 + a_7 \left(\left(\dfrac{x_2}{a_3} \right)^{a_4} - 1 \right) \right] y_1 - a_9 y_1 + a_8 a_{10} d \\ a_9(x_2 - x_3) - a_{10} d \end{bmatrix} - \begin{bmatrix} \dot{y}_1^* \\ \dot{y}_2^* \end{bmatrix}
$$

$$
+ \begin{bmatrix} a_6 a_8 \left[1 + a_7 \left(\left(\dfrac{x_2}{a_3} \right)^{a_4} - 1 \right) \right] & a_8 a_{11} \\ 0 & -a_{11} \end{bmatrix} \begin{bmatrix} h_1 \\ h_2 \end{bmatrix}
$$

$$
\equiv \begin{bmatrix} \mathcal{F}_1 \\ \mathcal{F}_2 \end{bmatrix} - \begin{bmatrix} \dot{y}_1^* \\ \dot{y}_2^* \end{bmatrix} + \begin{bmatrix} \mathcal{G}_{11} & \mathcal{G}_{12} \\ 0 & \mathcal{G}_{22} \end{bmatrix} \begin{bmatrix} h_1 \\ h_2 \end{bmatrix}.
\tag{23}
$$

According to first-order TSC [40] and dynamic surface control [26], the virtual control $h_d = [h_{d1}, h_{d2}]^T$ generated by the first-order filter and the virtual TSC $h_c = [h_{c1}, h_{c2}]^T$ including steady-state control $h_{cs} = [h_{cs1}, h_{cs2}]^T$, reference variation-based feedforward control $h_{cf} = [h_{cf1}, h_{cf2}]^T$ and error feedback control $h_{ce} = [h_{ce1}, h_{ce2}]^T$ are combined to form the first-layer control scheme, which is given by

$$
\begin{bmatrix} \tau_1 \dot{h}_{d1} + h_{d1} \\ \tau_2 \dot{h}_{d2} + h_{d2} \end{bmatrix} = \begin{bmatrix} h_{c1} \\ h_{c2} \end{bmatrix} = \begin{bmatrix} h_{cs1} \\ h_{cs2} \end{bmatrix} + \begin{bmatrix} h_{cf1} \\ h_{cf2} \end{bmatrix} + \begin{bmatrix} h_{ce1} \\ h_{ce2} \end{bmatrix},
\tag{24}
$$

where τ_1 and τ_2 are the time constants and

$$
\begin{bmatrix} h_{cs1} \\ h_{cs2} \end{bmatrix} = - \begin{bmatrix} \mathcal{G}_{11} & \mathcal{G}_{12} \\ 0 & \mathcal{G}_{22} \end{bmatrix}^{-1} \begin{bmatrix} \mathcal{F}_1 \\ \mathcal{F}_2 \end{bmatrix}, \begin{bmatrix} h_{cf1} \\ h_{cf2} \end{bmatrix} = \begin{bmatrix} \mathcal{G}_{11} & \mathcal{G}_{12} \\ 0 & \mathcal{G}_{22} \end{bmatrix}^{-1} \begin{bmatrix} \dot{y}_1^* \\ \dot{y}_2^* \end{bmatrix},
$$

$$
\begin{bmatrix} h_{ce1} \\ h_{ce2} \end{bmatrix} = - \begin{bmatrix} \mathcal{G}_{11} & \mathcal{G}_{12} \\ 0 & \mathcal{G}_{22} \end{bmatrix}^{-1} \begin{bmatrix} k_{11} s_{11} \\ k_{12} s_{12} \end{bmatrix}, \begin{bmatrix} h_{d1}(0) \\ h_{d2}(0) \end{bmatrix} = \begin{bmatrix} h_1(x_1(0), x_2(0)) \\ h_2(x_3(0), x_4(0)) \end{bmatrix},
$$

where k_{11} and k_{12} are the feedback control gains.

Layer 2: Given that the tracking error for h_d is

$$
S_2 = \begin{bmatrix} s_{21} \\ s_{22} \end{bmatrix} = \begin{bmatrix} h_1 - h_{d1} \\ h_2 - h_{d2} \end{bmatrix},
\tag{25}
$$

and the dynamics of S_2 is given by

$$
\dot{S}_2 = \begin{bmatrix} \dot{h}_1 - \dot{h}_{d1} \\ \dot{h}_2 - \dot{h}_{d2} \end{bmatrix} = \begin{bmatrix} \dfrac{\partial h_1}{\partial x_1}\dot{x}_1 + \dfrac{\partial h_1}{\partial x_2}\dot{x}_2 \\ \dfrac{\partial h_2}{\partial x_3}\dot{x}_3 + \dfrac{\partial h_2}{\partial x_4}\dot{x}_4 \end{bmatrix} - \begin{bmatrix} \dot{h}_{d1} \\ \dot{h}_{d2} \end{bmatrix}
$$

$$
= \begin{bmatrix} \dfrac{\partial h_1}{\partial x_1}\left(-a_1 x_1 - \dfrac{a_2}{x_1}\left(\left(\dfrac{x_2}{a_3} \right)^{a_4} - 1 \right) h_1 \right) + \dfrac{\partial h_1}{\partial x_2} a_6 \left[1 + a_7 \left(\left(\dfrac{x_2}{a_3} \right)^{a_4} - 1 \right) \right](h_1 - y_1) \\ \dfrac{\partial h_2}{\partial x_3}[a_9(x_2 - x_3) - a_{10}d - a_{11}h_2] - \dfrac{\partial h_2}{\partial x_4}\dfrac{x_4}{a_{12}} \end{bmatrix}
$$

$$
- \begin{bmatrix} \dot{h}_{d1} \\ \dot{h}_{d2} \end{bmatrix} + \begin{bmatrix} \dfrac{\partial h_1}{\partial x_1} a_5 & 0 \\ 0 & \dfrac{\partial h_2}{\partial x_4}\dfrac{1}{a_{12}} \end{bmatrix} \begin{bmatrix} u_1 \\ u_2 \end{bmatrix}
$$

$$
\equiv \begin{bmatrix} \mathcal{A}_1 \\ \mathcal{A}_2 \end{bmatrix} - \begin{bmatrix} \dot{h}_{d1} \\ \dot{h}_{d2} \end{bmatrix} + \begin{bmatrix} \mathcal{B}_1 & 0 \\ 0 & \mathcal{B}_2 \end{bmatrix} \begin{bmatrix} u_1 \\ u_2 \end{bmatrix}
\tag{26}
$$

where $\frac{\partial h_1}{\partial x_1} = \frac{30}{\pi} \left(p_1 + p_2 \frac{x_2}{a_3} + 2p_4 N_{cp} + 2p_6 N_{cp} \frac{x_2}{a_3} + p_7 \left(\frac{x_2}{a_3} \right)^2 \right)$,

$\frac{\partial h_1}{\partial x_2} = p_2 \frac{N_{cp}}{a_3} + p_3 \frac{1}{a_3} + 2p_5 \frac{x_2}{a_3^2} + p_6 \frac{N_{cp}^2}{a_3} + 2p_7 N_{cp} \frac{x_2}{a_3^2}$, $\frac{\partial h_2}{\partial x_3} = \sin^2\left(\frac{\pi}{180}x_4 \right)$ and

$\frac{\partial h_2}{\partial x_4} = \frac{\pi}{90}x_3 \sin\left(\frac{\pi}{180}x_4 \right)\cos\left(\frac{\pi}{180}x_4 \right)$.

The nonlinear TSC law is designed as

$$
u = \begin{bmatrix} u_1 \\ u_2 \end{bmatrix} = \begin{bmatrix} u_{s1} \\ u_{s2} \end{bmatrix} + \begin{bmatrix} u_{f1} \\ u_{f2} \end{bmatrix} + \begin{bmatrix} u_{e1} \\ u_{e2} \end{bmatrix},
\tag{27}
$$

where the steady-state control $u_s = [u_{s1}, u_{s2}]^T$, reference variation-based feedforward control $u_f = [u_{f1}, u_{f2}]^T$ and error feedback control $u_e = [u_{e1}, u_{e2}]^T$ are given as

$$
\begin{bmatrix} u_{s1} \\ u_{s2} \end{bmatrix} = - \begin{bmatrix} \mathcal{B}_1 & 0 \\ 0 & \mathcal{B}_2 \end{bmatrix}^{-1} \begin{bmatrix} \mathcal{A}_1 + \mathcal{G}_{11} s_{11} \\ \mathcal{A}_2 + \mathcal{G}_{12} s_{11} + \mathcal{G}_{22} s_{12} \end{bmatrix},
$$

$$
\begin{bmatrix} u_{f1} \\ u_{f2} \end{bmatrix} = \begin{bmatrix} \mathcal{B}_1 & 0 \\ 0 & \mathcal{B}_2 \end{bmatrix}^{-1} \begin{bmatrix} \dot{h}_{d1} \\ \dot{h}_{d2} \end{bmatrix}, \begin{bmatrix} u_{e1} \\ u_{e2} \end{bmatrix} = - \begin{bmatrix} \mathcal{B}_1 & 0 \\ 0 & \mathcal{B}_2 \end{bmatrix}^{-1} \begin{bmatrix} k_{21} s_{21} \\ k_{22} s_{22} \end{bmatrix},
$$

where $k_{21} > 0$ and $k_{22} > 0$.

Note that the dynamic surface TSC law in (27) does not involve model differentiation and thus has prevented the explosion of terms. The overall stability of the closed-loop system (11) with the proposed controller (24) and (27) will be shown in the following theorem.

Theorem 3.1 *Consider the system (11) and design the controller (24) and (27). Let there be a constant $\alpha > 0$ such that the following inequalities hold:*

$$
k_{11} - \frac{|\mathcal{G}_{11}| + |\mathcal{G}_{12}|}{2} \geq \frac{\alpha}{2}, \; k_{12} - \frac{|\mathcal{G}_{22}|}{2} \geq \frac{\alpha}{2}, \; k_{21} \geq \frac{\alpha}{2}, \; k_{22} \geq \frac{\alpha}{2},
$$

$$
\frac{1}{\tau_1} - \frac{|\mathcal{G}_{11}| + 1}{2} \geq \frac{\alpha}{2}, \; \frac{1}{\tau_2} - \frac{|\mathcal{G}_{12}| + |\mathcal{G}_{22}| + 1}{2} \geq \frac{\alpha}{2}.
\tag{28}
$$

Therefore, the control output signal is ISS and converges to a sufficiently small neighborhood of the reference, which yields a satisfactory tracking error.

Proof. Please refer to 0.1.

Remark 1 *Given that* $x_2 \in [x_{2,\min}, x_{2,\max}]$. $\mathcal{G}_{11}(x_2)$ *in* (28) *changes in a polytope as*

$$\mathcal{G}_{11}(x_2) = \lambda(x_2)\mathcal{G}_{11}(x_{2,\max}) + (1 - \lambda(x_2))\mathcal{G}_{11}(x_{2,\min}),$$
$$\lambda(x_2) = \frac{\mathcal{G}_{11}(x_2) - \mathcal{G}_{11}(x_{2,\min})}{\mathcal{G}_{11}(x_{2,\max}) - \mathcal{G}_{11}(x_{2,\min})} \in [0,1]. \tag{29}$$

Then, any time-invariant k_{11} *and* τ_1 *followed by the linear matrix inequalities (LMIs)*

$$k_{11} \geq \frac{\alpha}{2} + \frac{|\mathcal{G}_{11}(x_{2,\max})| + |\mathcal{G}_{12}|}{2}, \quad k_{11} \geq \frac{\alpha}{2} + \frac{|\mathcal{G}_{11}(x_{2,\min})| + |\mathcal{G}_{12}|}{2} \tag{30}$$

$$\frac{1}{\tau_1} \geq \frac{\alpha}{2} + \frac{|\mathcal{G}_{11}(x_{2,\max})| + 1}{2}, \quad \frac{1}{\tau_1} \geq \frac{\alpha}{2} + \frac{|\mathcal{G}_{11}(x_{2,\min})| + 1}{2} \tag{31}$$

satisfy the condition in (28).

Remark 2 *Compared with the traditional TSC approach [24,25] for PEMFCs, the key feature of the proposed TSC approach is that due to the presence of the auxiliary filter, none of the nonlinearities are ever differentiated more than once. This is a crucial point for PEMFCs because it not only reduces all the derivative errors of nonlinear MAPs during the design process but also helps industrial engineers understand high-order TSC algorithms in a hierarchical manner.*

Ultimately, the hierarchical structure of the dynamic surface TSC scheme for PEMFCs is depicted in Fig. 4.

Reconfigurable controller design

After FDI, fault accommodation and the reconfiguration mechanism determine which backup controller is activated. In this subsection, based on the proposed TSC, two backup controllers are designed to regulate the air flow rate and pressure of the cathode in the presence of valve locking in place and air leakage in the supply manifold.

FTC for valve stuck fault

According to the faulty model of (13) and (14), the PEMFC air supply system under the stuck fault is a SISO nonlinear model, of which the time derivatives of the tracking errors for y_1 and h_1 along dynamics can be respectively represented by the following equations:

$$\dot{s}_{11} = -a_6 a_8 \left[1 + a_7\left(\left(\frac{x_2}{a_3}\right)^{a_4} - 1\right)\right]y_1 - a_9 y_1 + a_8 a_{10} d + a_8 a_{11} h_2(x_3, f_1)$$
$$-\ddot{y}_1^* + a_6 a_8 \left[1 + a_7\left(\left(\frac{x_2}{a_3}\right)^{a_4} - 1\right)\right]h_1$$
$$\equiv \mathcal{F}_1(f_1) - \ddot{y}_1^* + \mathcal{G}_{11} h_1, \tag{32}$$

$$\dot{s}_{12} = \frac{\partial h_1}{\partial x_1}\dot{x}_1 + \frac{\partial h_1}{\partial x_2}\dot{x}_2 - \dot{h}_{d1} = \frac{\partial h_1}{\partial x_1}\left(-a_1 x_1 - \frac{a_2}{x_1}\left(\left(\frac{x_2}{a_3}\right)^{a_4} - 1\right)h_1\right)$$
$$+ \frac{\partial h_1}{\partial x_2} a_6 \left[1 + a_7\left(\left(\frac{x_2}{a_3}\right)^{a_4} - 1\right)\right](h_1 - y_1) - \dot{h}_{d1} + \frac{\partial h_1}{\partial x_1}a_5 u_1$$
$$= \mathcal{A}_1 - \dot{h}_{d1} + \mathcal{B}_{11} u_1, \tag{33}$$

where the stuck fault f_1 is assumed to be detected and estimated as a known disturbance.

For the PEMFC system, the strategy of dynamic surface TSC is illustrated in Fig. 4. Through a two-layer structure, a second-order TSC approach can be separated as two first-order TSC schemes together with a first-order filter. Thus, for the PEMFC system with a stuck fault, we design the following FTC scheme:

Layer 1:
$$\begin{cases} \tau_1 \dot{h}_{d1} + h_{d1} = h_{c1}, \ h_{d1}(0) = h_1(x_1(0), x_2(0)) \\ h_{c1} = h_{cs1} + h_{cf1} + h_{ce1} \\ h_{cs1} = -\mathcal{G}_{11}^{-1}\mathcal{F}_1(f_1) \\ h_{cf1} = \mathcal{G}_{11}^{-1}\ddot{y}_1^* \\ h_{ce1} = -\mathcal{G}_{11}^{-1}k_{11}s_{11} \end{cases} \tag{34}$$

Layer 2:
$$\begin{cases} u_1 = u_{s1} + u_{f1} + u_{e1} \\ u_{s1} = -\mathcal{B}_{11}^{-1}(\mathcal{A}_1 + \mathcal{G}_{11}s_{11}) \\ u_{f1} = \mathcal{B}_{11}^{-1}\dot{h}_{d1} \\ u_{e1} = -\mathcal{B}_{11}^{-1}k_{21}s_{21} \end{cases}$$

For analysis, the overall stability of the closed-loop system under a stuck fault is described in the following theorem.

Theorem 3.2 *Considering the faulty system (13), there exists a scalar* $\alpha > 0$ *such that*

$$k_{11} - \frac{|\mathcal{G}_{11}|}{2} \geq \frac{\alpha}{2}, \ k_{21} \geq \frac{\alpha}{2}, \ \frac{1}{\tau_1} - \frac{|\mathcal{G}_{11}| + 1}{2} \geq \frac{\alpha}{2}. \tag{35}$$

The proposed TSC (34) can render the controlled output y_1 *to track the time-varying reference* y_1^* *asymptotically in the presence of the valve stuck fault* f_1.
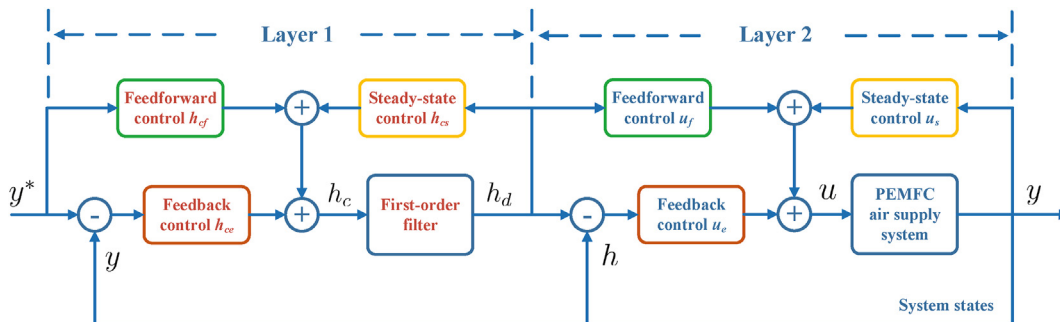

Fig. 4 – **Schematic diagram of the dynamic surface TSC law.**

Proof. Please vrefer to 0.2.

FTC *for supply manifold leakage fault*

Different from the valve stuck case, the leakage fault f_2 at the supply manifold cannot be measured directly, such that fault estimation and accommodation are not trivial. According to (17), where the measurements of y_1, x_2 and x_3 are available, the fault estimator is designed as follows:

$$\dot{\widehat{f}}_2 = -l_1 [y_1 - a_8(x_2 - x_3) + \widehat{f}_2],\qquad(36)$$

where $l_1 > 0$ and $\widehat{f}_2$ is denoted as the estimated value of the leakage fault. Define the estimate error $e_3 = f_2 - \widehat{f}_2$ and deduce the dynamics of e_3 as

$$\dot{e}_3 = \dot{f}_2 + l_1 [y_1 - a_8(x_2 - x_3) - \widehat{f}_2] = -l_1 e_3 + \dot{f}_2.\qquad(37)$$

then, the dynamics of the tracking errors for y and h along (16) and (17) are given as
and

$$
\begin{aligned}
\dot{S}_1 &= \begin{bmatrix} \dot{y}_1 - \dot{y}_1^* \\ \dot{y}_2 - \dot{y}_2^* \end{bmatrix} = \begin{bmatrix} a_8 \dot{x}_2 - a_8 \dot{x}_3 - \dot{f}_2 - \dot{y}_1^* \\ \dot{y}_2 - \dot{y}_2^* \end{bmatrix} \\
&= \begin{bmatrix} -a_6 a_8 \left[1 + a_7 \left(\left(\frac{x_2}{a_3} \right)^{a_4} - 1 \right) \right] a_8(x_2 - x_3) - a_8 a_9(x_2 - x_3) + a_8 a_{10} d \\ a_9(x_2 - x_3) - a_{10} d \end{bmatrix} - \begin{bmatrix} \dot{y}_1^* \\ \dot{y}_2^* \end{bmatrix} \\
&\quad + \begin{bmatrix} a_6 a_8 \left[1 + a_7 \left(\left(\frac{x_2}{a_3} \right)^{a_4} - 1 \right) \right] & a_8 a_{11} \\ 0 & -a_{11} \end{bmatrix} \begin{bmatrix} h_1 \\ h_1 \end{bmatrix} + \begin{bmatrix} a_8 a_{13} & -1 \\ -a_{13} & 0 \end{bmatrix} \begin{bmatrix} f_2 \\ \dot{f}_2 \end{bmatrix} \\
&\equiv \begin{bmatrix} \mathcal{F}_1 \\ \mathcal{F}_2 \end{bmatrix} - \begin{bmatrix} \dot{y}_1^* \\ \dot{y}_2^* \end{bmatrix} + \begin{bmatrix} \mathcal{G}_{11} & \mathcal{G}_{12} \\ 0 & \mathcal{G}_{22} \end{bmatrix} \begin{bmatrix} h_1 \\ h_2 \end{bmatrix} + \begin{bmatrix} \mathcal{H}_1 & -1 \\ \mathcal{H}_2 & 0 \end{bmatrix} \begin{bmatrix} f_2 \\ \dot{f}_2 \end{bmatrix},
\end{aligned}
\qquad(38)
$$

$$
\begin{aligned}
\dot{S}_2 &= \begin{bmatrix} \dot{h}_1 - \dot{h}_{d1} \\ \dot{h}_2 - \dot{h}_{d2} \end{bmatrix} = \begin{bmatrix} \frac{\partial h_1}{\partial x_1} \dot{x}_1 + \frac{\partial h_1}{\partial x_2} \dot{x}_2 \\ \frac{\partial h_2}{\partial x_3} \dot{x}_3 + \frac{\partial h_2}{\partial x_4} \dot{x}_4 \end{bmatrix} - \begin{bmatrix} \dot{h}_{d1} \\ \dot{h}_{d2} \end{bmatrix} \\
&= \begin{bmatrix} \left(\frac{\partial h_1}{\partial x_1} \left(-a_1 x_1 - \frac{a_2}{x_1} \left(\left(\frac{x_2}{a_3} \right)^{a_4} - 1 \right) h_1 \right) \\ + \frac{\partial h_1}{\partial x_2} a_6 \left[1 + a_7 \left(\left(\frac{x_2}{a_3} \right)^{a_4} - 1 \right) \right] (h_1 - a_8(x_2 - x_3)) \right) \\ \frac{\partial h_2}{\partial x_3} [a_9(x_2 - x_3) - a_{10} d - a_{11} h_2] - \frac{\partial h_2}{\partial x_4} \frac{x_4}{a_{12}} \end{bmatrix} \\
&\quad - \begin{bmatrix} \dot{h}_{d1} \\ \dot{h}_{d2} \end{bmatrix} + \begin{bmatrix} \frac{\partial h_1}{\partial x_1} a_5 & 0 \\ 0 & \frac{\partial h_2}{\partial x_4} \frac{1}{a_{12}} \end{bmatrix} \begin{bmatrix} u_1 \\ u_2 \end{bmatrix} + \begin{bmatrix} 0 \\ -\frac{\partial h_2}{\partial x_3} a_{13} \end{bmatrix} f_2 \\
&\equiv \begin{bmatrix} \mathcal{A}_1 \\ \mathcal{A}_2 \end{bmatrix} - \begin{bmatrix} \dot{h}_{d1} \\ \dot{h}_{d2} \end{bmatrix} + \begin{bmatrix} \mathcal{B}_1 & 0 \\ 0 & \mathcal{B}_2 \end{bmatrix} \begin{bmatrix} u_1 \\ u_2 \end{bmatrix} + \begin{bmatrix} 0 \\ \mathcal{C}_2 \end{bmatrix} f_2.
\end{aligned}
\qquad(39)
$$

Based on the results in (36)-(39), the FTC for the leakage faulty case using the dynamic surface triple-step approach is given as

Layer 1:
$$
\begin{cases}
\begin{bmatrix} \tau_1 \dot{h}_{d1} + h_{d1} \\ \tau_2 \dot{h}_{d2} + h_{d2} \end{bmatrix} = \begin{bmatrix} h_{c1} \\ h_{c2} \end{bmatrix}, \begin{bmatrix} h_{d1}(0) \\ h_{d2}(0) \end{bmatrix} = \begin{bmatrix} h_1(x_1(0), x_2(0)) \\ h_2(x_3(0), x_4(0)) \end{bmatrix} \\[2ex]
\begin{bmatrix} h_{c1} \\ h_{c2} \end{bmatrix} = \begin{bmatrix} h_{cs1} \\ h_{cs2} \end{bmatrix} + \begin{bmatrix} h_{cf1} \\ h_{cf2} \end{bmatrix} + \begin{bmatrix} h_{ce1} \\ h_{ce2} \end{bmatrix} \\[2ex]
\begin{bmatrix} h_{cs1} \\ h_{cs2} \end{bmatrix} = -\begin{bmatrix} \mathcal{G}_{11} & \mathcal{G}_{12} \\ 0 & \mathcal{G}_{22} \end{bmatrix}^{-1} \begin{bmatrix} \mathcal{F}_1 + \mathcal{H}_1 \widehat{f}_2 \\ \mathcal{F}_2 + \mathcal{H}_2 \widehat{f}_2 \end{bmatrix} \\[2ex]
\begin{bmatrix} h_{cf1} \\ h_{cf2} \end{bmatrix} = \begin{bmatrix} \mathcal{G}_{11} & \mathcal{G}_{12} \\ 0 & \mathcal{G}_{22} \end{bmatrix}^{-1} \begin{bmatrix} \dot{y}_1^* \\ \dot{y}_2^* \end{bmatrix} \\[2ex]
\begin{bmatrix} h_{ce1} \\ h_{ce2} \end{bmatrix} = -\begin{bmatrix} \mathcal{G}_{11} & \mathcal{G}_{12} \\ 0 & \mathcal{G}_{22} \end{bmatrix}^{-1} \begin{bmatrix} k_{11} s_{11} \\ k_{12} s_{12} \end{bmatrix}
\end{cases}
$$

Layer 2:
$$
\begin{cases}
\begin{bmatrix} u_1 \\ u_2 \end{bmatrix} = \begin{bmatrix} u_{s1} \\ u_{s2} \end{bmatrix} + \begin{bmatrix} u_{f1} \\ u_{f2} \end{bmatrix} + \begin{bmatrix} u_{e1} \\ u_{e2} \end{bmatrix} \\[2ex]
\begin{bmatrix} u_{s1} \\ u_{s2} \end{bmatrix} = -\begin{bmatrix} \mathcal{B}_1 & 0 \\ 0 & \mathcal{B}_2 \end{bmatrix}^{-1} \begin{bmatrix} \mathcal{A}_1 + \mathcal{G}_{11} s_{11} \\ \mathcal{A}_2 + \mathcal{C}_2 \widehat{f}_2 + \mathcal{G}_{12} s_{11} + \mathcal{G}_{22} s_{12} \end{bmatrix} \\[2ex]
\begin{bmatrix} u_{f1} \\ u_{f2} \end{bmatrix} = \begin{bmatrix} \mathcal{B}_1 & 0 \\ 0 & \mathcal{B}_2 \end{bmatrix}^{-1} \begin{bmatrix} \dot{h}_{d1} \\ \dot{h}_{d2} \end{bmatrix} \\[2ex]
\begin{bmatrix} u_{e1} \\ u_{e2} \end{bmatrix} = -\begin{bmatrix} \mathcal{B}_1 & 0 \\ 0 & \mathcal{B}_2 \end{bmatrix}^{-1} \begin{bmatrix} k_{21} s_{21} \\ k_{22} s_{22} \end{bmatrix}
\end{cases}
$$

(40)

where the control gains k_{ij} with $i, j = 1, 2$, the filter parameters τ_i with $i = 1, 2$ and the fault estimator gain l_1 are synthesized based on the conditions of the following theorem.

Theorem 3.3 *Consider the faulty system given by* (16) *and* (17). *Construct the fault estimator* (36) *and the FTC scheme given by* (40). *Design the parameters* k_{ij}, τ_i *and* l_1 *satisfying the following inequalities:*

$$k_{11} - 2 \geq \frac{\alpha}{2}, \quad k_{12} - 1 \geq \frac{\alpha}{2}, \quad k_{21} - \frac{1}{2} \geq \frac{\alpha}{2}, \quad k_{22} \geq \frac{\alpha}{2},$$

$$\frac{1}{\tau_1} - \frac{\mathcal{G}_{11}^2 + 1}{2} \geq \frac{\alpha}{2}, \quad \frac{1}{\tau_2} - \frac{\mathcal{G}_{12}^2 + \mathcal{G}_{22}^2 + 1}{2} \geq \frac{\alpha}{2}, \qquad (41)$$

$$l_1 - \frac{\mathcal{H}_1^2 + \mathcal{H}_2^2 + \mathcal{C}_2^2 + 1}{2} \geq \frac{\alpha}{2}.$$

Given that the fault f_2 and its derivative $\dot{f}_2$ are bounded, the control output signal is ISS and converges to a sufficiently small neighborhood of the reference as $\dot{f}_2 \to 0$.

Proof. Please refer to 0.3.

Finally, the proposed FTC strategy for the PEMFC is illustrated in Fig. 5, which is composed of four modules for fault detection and diagnosis, fault accommodation and reconfiguration mechanism and the proposed dynamic surface TSC. Due to space limitations, the fault diagnosis and reconfiguration mechanism is briefly described by using the simulation cases in the following section.

Remark 3 *Lower controllers are usually preferable in terms of implementation and computing efforts. Note that the arithmetic operations in each step of the proposed FTCs are 119, 90 and 123, in that order, which is acceptable, for example, for embedded controllers (e.g., National Instruments CompactRIO). In addition, the calculation cost of steady-state control (79.0% of the total) can be saved by lookup tables, and the continuous-time controllers are converted to discrete-time controllers for implementation.*

Remark 4 *One of the main challenges related to implementation of the proposed control algorithm for a real system is the modeling and validation of PEMFCs. Although the steady map of the flow rate and the parameters of the valve are calibrated by experimental data, validation of the whole PEMFC model [12] still needs more experimental conditions and efforts. To compensate air leakage, hardware measurements of the flow rate and the pressure in the cathode can be realized by air flow and pressure sensors (e.g., CAFS1000 and GemsSensor3500), respectively. When the measurements are restricted in automotive operations, more contributions on virtual sensors or model-based observers [43] are expected in the future.*

Remark 5 *Possible causes of a throttle becoming stuck may include a faulty throttle body, dirty throttle plate or linkage, or faulty throttle sensors and actuators. While the FTC algorithm in Theorem 2 allows for maintaining the original inlet flow rate, the tradeoff is the loss of pressure control in the cathode. Note that the pressure of the anode normally follows the pressure of the cathode and is proportional to the current load [5]. Hence, the management system of the PEMFC should cooperate with its control law to reduce the reference value of the current load and maintain the specified operations of the PEMFC system.*

Remark 6 *Cathode leakage from the stack may come from failure of the gas expander to the inlet of the stack, causing overpressure of air inside the stack channels or intensified stack aging by mechanical, thermal and chemical degradation [44]. To compensate for cathode leakage, it is necessary to detect the leak and stop the source of the leak for system safety. During the faulty period, the FTC algorithm in Theorem 3 is used to maintain the control performance.*

Simulation results

This section presents the simulation results conducted to verify the effectiveness of the proposed FTC scheme on a high-fidelity PEMFC model [12]. The physical parameters used in the simulation are given in Table 1.

There are four major subsystems in a typical PEMFC system: the air supply subsystem for the cathode, the hydrogen supply subsystem for the anode, the water and heat management subsystem, and the energy management subsystem. Oxygen from the cathode reacts electrochemically with hydrogen from the anode to power the load under a proper humidity and temperature environment. Therefore, in the simulation, it is set that the hydrogen tank at the anode side is capable of instantaneously providing the required amount of hydrogen, and both air and hydrogen streams are humidified to reach the required amount of water for correct operation of the stack. To improve the validity of the simulation, both measurement and process noises are considered; i.e., the compressor speed, the air supply manifold pressure, the cathode pressure, the inlet flow rate at the cathode, the
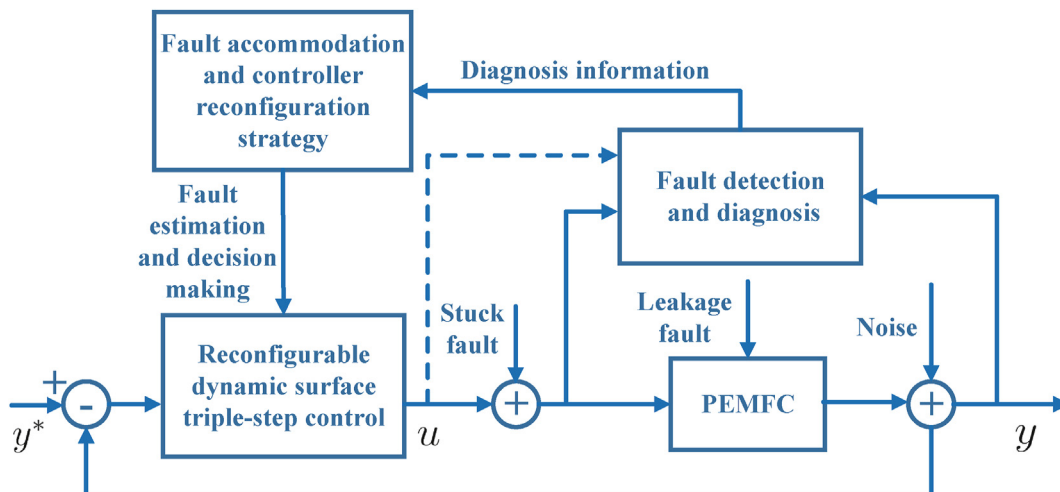

Fig. 5 – Schematic diagram of the proposed FTC scheme for PEMFCs.

Symbol	Description	Value	Unit
	Table 1 – Physical parameters of the PEMFC system.		
J_{cp}	Compressor inertia	5×10^{-5}	$kg \cdot m^2$
R_{cm}	Compressor resistance	0.9	Ω
η_{cm}	Mechanical efficiency	90	%
k_t	Motor constant	0.0153	V/(rad/sec)
k_v	Motor constant	0.0153	Nm/Amp
C_p	Specific heat capacity	1004	J/kg/K
T_{at}	Atmosphere temperature	298.15	K
η_{cp}	Maximum efficiency of compressor	80	%
γ	Ratio of specific heat	1.4	–
p_{at}	Atmospheric pressure	101315	Pa
R_a	Air gas constant	298.6	J/kg/K
V_{sm}	Volume of air supply manifold	0.02	m^3
k_{sm}	Flow constant	3.629×10^{-6}	kg/s/Pa
R_{O_2}	Oxygen gas constant	259.8	J/kg/K
M_{O_2}	Oxygen molar mass	0.032	kg/mol
V_{ca}	Volume of cathode	0.01	m^3
T_{st}	Temperature of cathode	353.15	K
n_{cell}	Number of cells	381	–
F	Faraday number	96485	–
$C_{D,tr}$	Throttle discharge coefficient	0.0248	–
$A_{T,tr}$	Maximum throttle opening area	0.002	m^2
R	Universal gas constant	8.3145	J/mol/K
T_s	Time constant of throttle	0.04	–

throttle opening angle and the load current are assumed to be contaminated with noise ($s/n = 10$). Through continuous simulation tests, the parameters of the proposed control scheme are chosen as follows:

$$k_{11} = 252, \ k_{12} = 57, \ k_{21} = 536, \ k_{22} = 113, \ \tau_1 = 0.01, \ \tau_2 = 0.01, \ l_1 = 10.$$

In the following, three situations are separately presented and discussed to validate the performance of the proposed fault-tolerance controllers. The first scenario investigates the PEMFC performance under normal operation. The second scenario illustrates the PEMFC performance when a stuck fault of the back pressure valve occurs. The last scenario analyzes the case of supply manifold leakage.

Fault scenario 1: Normal

To test the validation of the proposed control strategy, different load variations between 100 A and 300 A are shown in Fig. 6 (a). For the fault-free case, the nominal controller in (24) and (27) is selected and implemented in the PEMFC dynamic model to regulate the inlet flow rate and pressure in the cathode.

The corresponding flow rate and pressure transients are plotted in Fig. 6 (b) and (c), respectively. By manipulating the compressor voltage and throttle angle commands, the nominal controller successfully maintains the tracking error of the cathode inlet flow rate at zero, and the pressure of the cathode well follows the desired value adjusted by the load current. Fig. 6 (d), (e) and (f) present the recorded state responses of the compressor speed, air supply manifold pressure and throttle opening angle under load variations, respectively. The simulation results of the control inputs that are plotted in Fig. 6 (g) and (h) are maintained in a reasonable region. Fig. 6 (i) shows

the control trajectory of the oxygen excess ratio, from which we can find that the oxygen excess ratio under the normal case is satisfactory under the time-varying trajectory of the load current, and thus, the effectiveness of the proposed controller is identified.

Fault scenario 2: back pressure valve stuck

To investigate the control performance of the proposed FTC strategy under faulty conditions, the PEMFC air supply system has been damaged by introducing a back pressure valve stuck fault at 10 s. In this case, by monitoring and comparing the throttle opening angle with the command value of this angle, the fault detection and diagnosis module is realized.

The load current change is set as a sinusoidal signal, as shown in Fig. 7 (a), and the simulation results of the normal controller (abbreviated by TSC) and the proposed FTC approach are given in Fig. 7 (b)–(i). At $t = 10$ s, the fault diagnosis module detects the valve stuck fault and then triggers the reconfiguration mechanism algorithm to reconstruct and activate the backup controller (34) to maintain the stability and performance of the PEMFC system.

Fig. 7 (b) compares the cathode inlet flow rates controlled by the FTC algorithm with the normal TSC algorithm, where the solid and dashed-dotted lines indicate the control output y_1 by the proposed controller and the normal controller, respectively. Note that the tracking performance between the two control strategies is obviously different: The flow rate of the FTC-aided PEMFC is close to the reference value, even if a stuck fault exists, whereas the flow rate of the PEMFC without FTC cannot follow the reference as soon as the stuck fault is introduced. Similar phenomena can be seen in the state and input results, which are plotted in Fig. 7 (d)–(h). From Fig. 7 (c), the control result of the cathode pressure of the TSC-aided
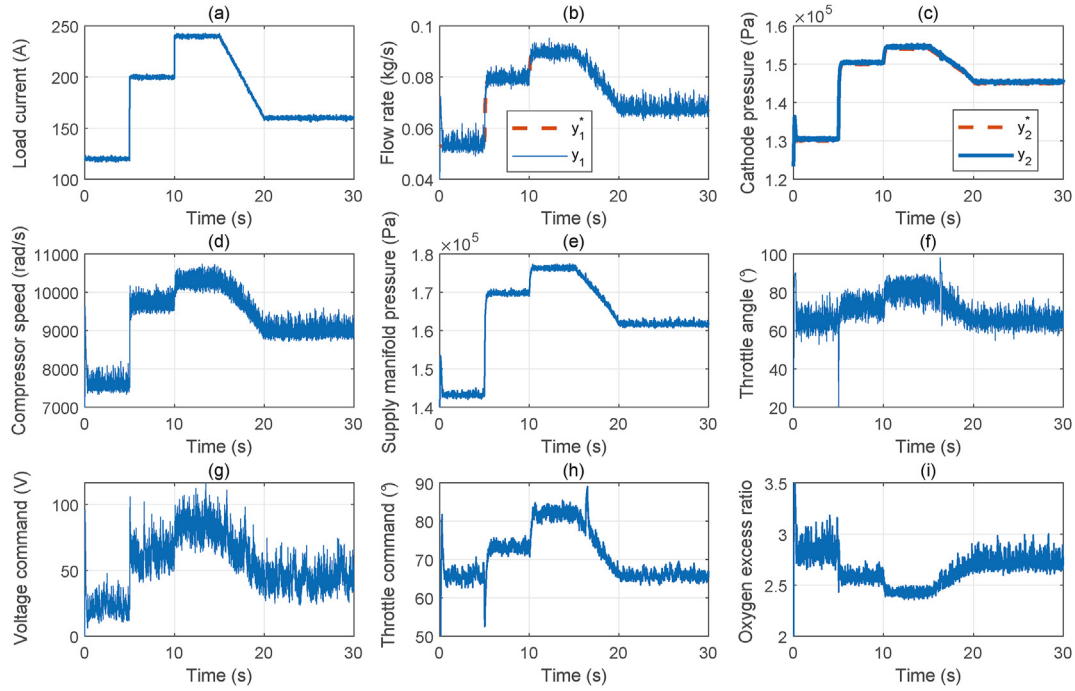
Fig. 6 − Simulation results in the normal case. (a) Load current. (b) Cathode inlet flow rate and reference. (c) Cathode pressure and reference. (d) Compressor speed. (e) Supply manifold pressure. (f) Throttle opening angle. (g) Voltage command. (h) Throttle angle command. (i) Oxygen excess ratio.
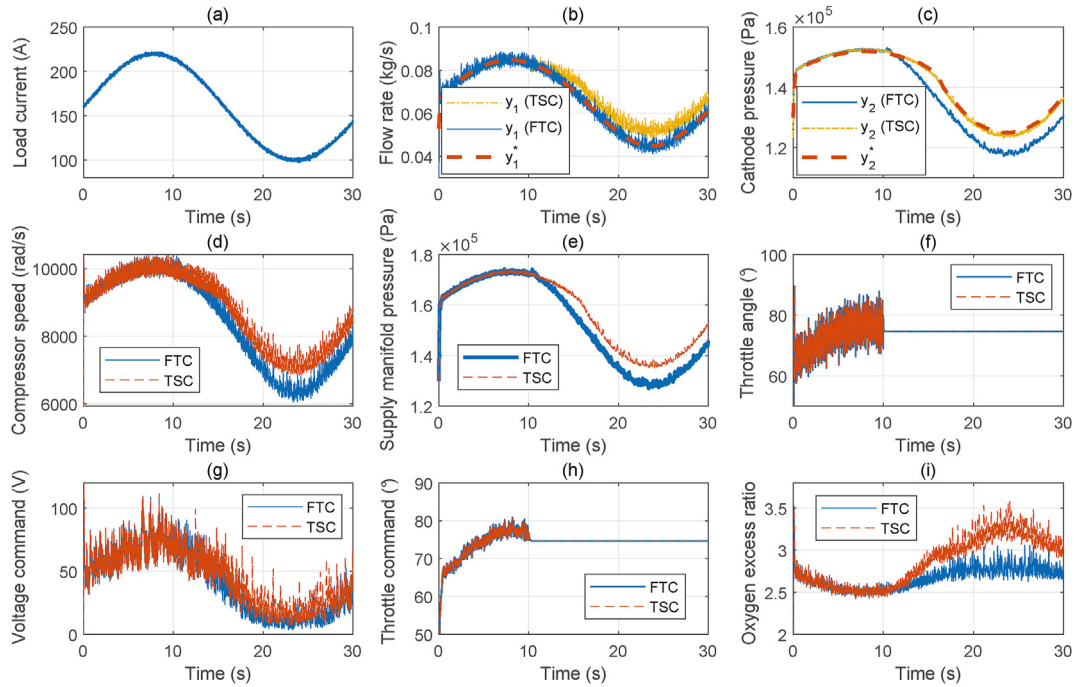

Fig. 7 − Simulation results in the stuck fault case. (a) Load current. (b) Cathode inlet flow rates and reference. (c) Cathode pressures and reference. (d) Compressor speeds. (e) Supply manifold pressures. (f) Throttle opening angles. (g) Voltage commands. (h) Throttle angle commands. (i) Oxygen excess ratios.

PEMFC is smaller than that with FTC. This is because the latter scheme compromises tracking the double objectives as desired due to the actuator fault. The oxygen excess ratios in the two control algorithms are compared in Fig. 7 (i), by which the effectiveness of the proposed FTC scheme can be verified from the regulation of the oxygen excess ratio.
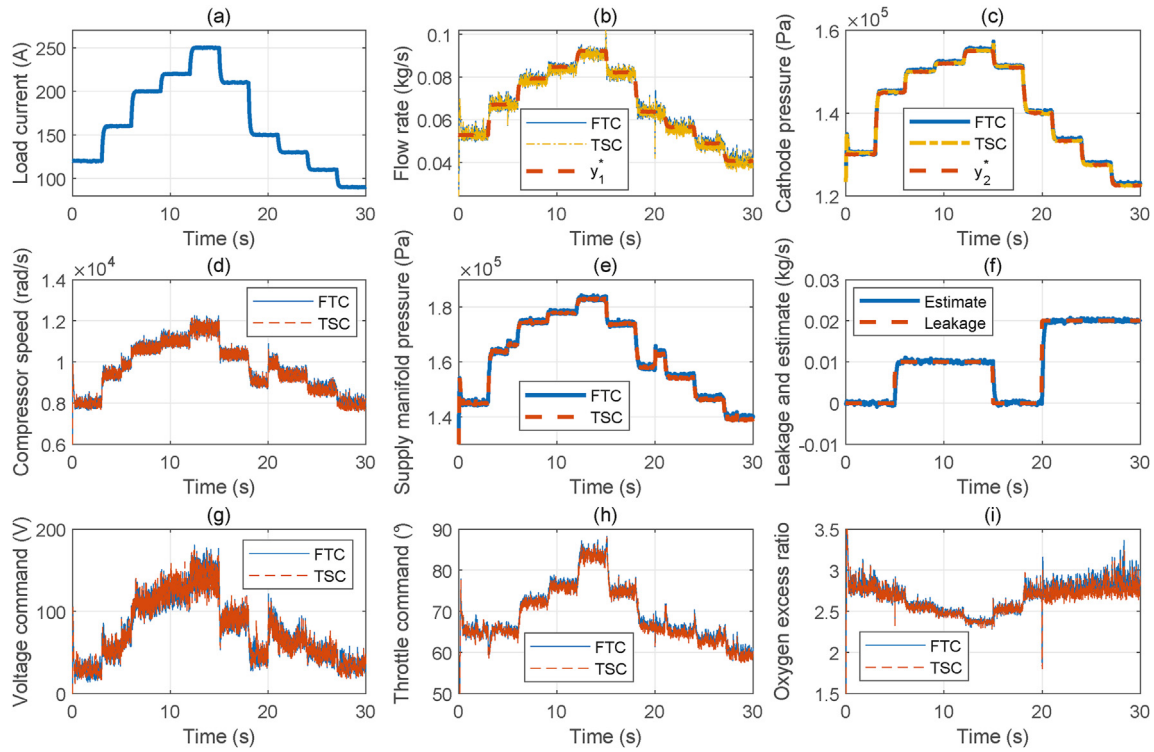
Fig. 8 – Simulation results in the leakage fault case. (a) Load current. (b) Cathode inlet flow rates and reference. (c) Cathode pressures and reference. (d) Compressor speeds. (e) Supply manifold pressures. (f) Leakage fault and its estimate. (g) Voltage commands. (h) Throttle angle commands. (i) Oxygen excess ratios.

Fault scenario 3: Supply manifold leakage

The last group of simulations is conducted to verify the fault estimation and active FTC performance of the modified TSC approach (40) against the supply manifold leakage fault. A piecewise changing sequence of the load current from 120 A to 280 A and to 120 A is employed, as shown in Fig. 8 (a). To simulate the supply manifold leakage scenario, a step fault with amplitude $f_2 = 0.01$ kg/s is injected into the supply manifold at 5 s with the last time 10 s. Further, the intermittent fault is activated at 20 s with amplitude $f_2 = 0.02$ kg/s and exists until the end of the simulation.

The response results of the control outputs, i.e., the flow rate into the cathode $W_{ca,in}$ and the pressure p_{ca} in the cathode, with respect to the current-dependent references are shown in Fig. 8 (b) and (c), respectively. Again, Fig. 8 (f) presents the estimation results of the leakage fault based on (36). From these three figures, both outputs could be well controlled because the estimator supports an accurate fault accommodation effort. The state values of the compressor speed and supply manifold pressure are plotted in Fig. 8 (d) and (e), respectively. The actuator effects of the voltage and throttle angle are shown in Fig. 8 (g) and (h), respectively. Furthermore, the oxygen excess ratios in the PEMFC are shown in Fig. 8 (i), by which the effectiveness of the proposed FTC scheme can be verified.

In addition, Fig. 8 (b)–(e) and Figs. (g)-(i) show a comparison of the response results with the specific FTC strategy (40) for leakage faults and the dynamic surface TSC (27). One can see that the normal controller maintains the PEMFC air-feed tracking well without knowledge of the leakage fault. The reason is that the proposed TSC approach works as a passive FTC strategy that is robust against the supply manifold leakage fault. Accordingly, neither FDI tools nor reconfiguration mechanisms are needed. However, the parameters of the passive FTC scheme cannot be adjusted with the faulty condition and tolerance is limited to some specific presumed faults (the stuck fault is excluded for TSC). Therefore, as shown in Fig. 5, active FTC with FDI and a reconfiguration mechanism is more feasible to benefit control stability and performance in practice.

Conclusion

A dynamic surface triple-step FTC scheme was proposed to realize integrated control of the air flow rate and pressure in an automotive PEMFC air supply system under normal, valve stuck and supply manifold leakage scenarios. This control scheme combined TSC with a dynamic surface to prevent the explosion of terms (compared to standard TSC). In addition, the control scheme employed Lyapunov design

to make PEMFCs tolerant to unexpected faults such as pipeline gas leaks and valve locking and to allow switching from a nominal controller to fault-tolerant controllers for faulty conditions. It is a high-confidence method in the sense that robustly asymptotic stability holds for PEMFCs. Numerical simulations using a high-fidelity PEMFC model were carried out to verify the effectiveness of the developed controllers.

However, much conservation might have been introduced since this paper does not consider thermal and water management in PEMFCs [41,42]. In addition, due to commercial cost, the cathode pressure of PEMFCs cannot be measured directly [25], but this problem has not yet been considered in the existing algorithms. Therefore, designing a soft sensor-based FTC scheme for PEMFC systems and performing experimental validation through real tests will be investigated in future research.

Declaration of competing interest

The authors declare that they have no known competing financial interests or personal relationships that could have appeared to influence the work reported in this paper.

Acknowledgments

Appendix

Proof of Theorem 1.

For the closed-loop system (11), (24) and (27), define the error of the boundary layer as $E_1 = \begin{bmatrix} e_1 & e_2 \end{bmatrix}^T = \begin{bmatrix} h_{d1} - h_{c1} & h_{d2} - h_{c2} \end{bmatrix}^T$ and the Lyapunov function candidate as

$$V_1 = \frac{1}{2}\left(s_{11}^2 + s_{12}^2 + s_{21}^2 + s_{22}^2\right) + \frac{1}{2}\left(e_1^2 + e_2^2\right), \qquad (.1)$$

Accordingly, differentiate (1), substituting (23) and (26), and perform some trivial algebraic manipulations:

$$\begin{aligned}
\dot{V}_1 &= s_{11}\dot{s}_{11} + s_{12}\dot{s}_{12} + s_{21}\dot{s}_{21} + s_{22}\dot{s}_{22} + e_1\dot{e}_1 + e_2\dot{e}_2 \\
&= s_{11}\left(\mathcal{F}_1 - \dot{y}_1^* + \mathcal{G}_{11}h_1 + \mathcal{G}_{12}h_2\right) + s_{12}\left(\mathcal{F}_2 - \dot{y}_2^* + \mathcal{G}_{22}h_2\right) \\
&\quad + s_{21}\left(\mathcal{A}_1 - \dot{h}_{d1} + \mathcal{B}_1 u_1\right) + s_{22}\left(\mathcal{A}_2 - \dot{h}_{d2} + \mathcal{B}_2 u_2\right) \\
&\quad + e_1\left(-\frac{1}{\tau_1}e_1 - \dot{h}_{c1}\right) + e_2\left(-\frac{1}{\tau_2}e_2 - \dot{h}_{c2}\right) \\
&= s_{11}\left(\mathcal{F}_1 - \dot{y}_1^* + \mathcal{G}_{11}h_{c1} + \mathcal{G}_{12}h_{c2}\right) + s_{12}\left(\mathcal{F}_2 - \dot{y}_2^* + \mathcal{G}_{22}h_{c2}\right)
\end{aligned}$$

$$\begin{aligned}
&\quad + s_{11}\mathcal{G}_{11}(s_{21} + e_1) + s_{11}\mathcal{G}_{12}(s_{22} + e_2) + s_{12}\mathcal{G}_{22}(s_{22} + e_2) \\
&\quad + s_{21}\left(\mathcal{A}_1 - \dot{h}_{d1} + \mathcal{B}_1 u_1\right) + s_{22}\left(\mathcal{A}_2 - \dot{h}_{d2} + \mathcal{B}_2 u_2\right) \\
&\quad + e_1\left(-\frac{1}{\tau_1}e_1 - \dot{h}_{c1}\right) + e_2\left(-\frac{1}{\tau_2}e_2 - \dot{h}_{c2}\right) \\
&= -k_{11}s_{11}^2 - k_{12}s_{12}^2 + s_{21}\left(\mathcal{G}_{11}s_{11} + \mathcal{A}_1 - \dot{h}_{d1} + \mathcal{B}_1 u_1\right) \\
&\quad + s_{22}\left(\mathcal{G}_{12}s_{11} + \mathcal{G}_{22}s_{12} + \mathcal{A}_2 - \dot{h}_{d2} + \mathcal{B}_2 u_2\right) \\
&\quad + e_1\left(\mathcal{G}_{11}s_{11} - \frac{1}{\tau_1}e_1 - \dot{h}_{c1}\right) + e_2\left(\mathcal{G}_{12}s_{11} + \mathcal{G}_{22}s_{12} - \frac{1}{\tau_2}e_2 - \dot{h}_{c2}\right) \\
&= -k_{11}s_{11}^2 - k_{12}s_{12}^2 - k_{21}s_{21}^2 - k_{22}s_{22}^2 \\
&\quad + e_1\left(\mathcal{G}_{11}s_{11} - \frac{1}{\tau_1}e_1 - \dot{h}_{c1}\right) + e_2\left(\mathcal{G}_{12}s_{11} + \mathcal{G}_{22}s_{12} - \frac{1}{\tau_2}e_2 - \dot{h}_{c2}\right)
\end{aligned}$$

$$(.2)$$

By using Young's inequality and the inequalities in (28), we finally obtain

$$\begin{aligned}
\dot{V}_1 &\le -\left(k_{11} - \frac{|\mathcal{G}_{11}| + |\mathcal{G}_{12}|}{2}\right)s_{11}^2 - \left(k_{12} - \frac{|\mathcal{G}_{22}|}{2}\right)s_{12}^2 - k_{21}s_{21}^2 - k_{22}s_{22}^2 \\
&\quad -\left(\frac{1}{\tau_1} - \frac{|\mathcal{G}_{11}| + 1}{2}\right)e_1^2 - \left(\frac{1}{\tau_2} - \frac{|\mathcal{G}_{12}| + |\mathcal{G}_{22}| + 1}{2}\right)e_2^2 + \beta_1 \\
&\le -\frac{1}{2}\alpha\left(s_{11}^2 + s_{12}^2 + s_{21}^2 + s_{22}^2 + e_1^2 + e_2^2\right) + \beta_1 = -\alpha V_1 + \beta_1,
\end{aligned}$$

$$(.3)$$

where $\beta_1 = \frac{1}{2}[\dot{h}_{c1}, \dot{h}_{c2}][\dot{h}_{c1}, \dot{h}_{c2}]^T$ is an unknown but bounded variable in practice. Inequality (0.3) implies that $\dot{V}_1 < 0$ on $\Omega_\gamma = \left\{x_e = [S_1, S_2, e]^T : V_1(x_e) \le \gamma\right\}$ when $\alpha \ge \frac{\beta_1}{\gamma}$. Thus, Ω_γ is an invariant set, that is, if $V_1(t_0) \le \gamma$, then $V_1(t) \le \gamma$ for all $t \ge t_0$. Therefore, the control output signal is ISS. Moreover, solving (0.3) yields

$$0 \le V_1(t) \le \frac{\beta_1}{\alpha} + \left[V_1(0) + \frac{\beta_1}{\alpha}\right]e^{-\alpha t}. \qquad (.4)$$

Taking the limit of (0.4) as $t \to \infty$, we have that $\lim_{t \to \infty} V_1(t) \le \frac{\beta_1}{\alpha}$, which, with (0.1), gives that $\|y - y^*\| \le \sqrt{\frac{2\beta_1}{\alpha}}$. Considering (28), we can choose $\tau_i > 0$, $i = 1, 2$ small enough and $k_{ij} > 0$, $i, j = 1, 2$ large enough to make α larger and thus to obtain an arbitrarily small $\frac{\beta_1}{\alpha}$, which, in turn, yields a satisfactory tracking error. The proof is done.

Proof of Theorem 2.

The asymptotic stability of the closed-loop system will be proved in the following analysis, provided that the fault information and the tracking reference satisfy the required conditions in Theorem 3.2. A Lyapunov function can be constructed as

$$V_2 = \frac{1}{2}\left(s_{11}^2 + s_{21}^2\right) + \frac{1}{2}e_1^2 \qquad (.5)$$

whose time derivative can be expressed as

$$\begin{aligned}
\dot{V}_2 &= s_{11}\dot{s}_{11} + s_{21}\dot{s}_{21} + e_1\dot{e}_1 \\
&= s_{11}\left(\mathcal{F}_1 - \dot{y}_1^* + \mathcal{G}_{11}h_1\right) + s_{21}\left(\mathcal{A}_1 - \dot{h}_{d1} + \mathcal{B}_1 u_1\right) \\
&\quad + e_1\left(-\frac{1}{\tau_1}e_1 - \dot{h}_{c1}\right) = s_{11}\left(\mathcal{F}_1 - \dot{y}_1^* + \mathcal{G}_{11}h_{c1}\right) \\
&\quad + s_{21}\left(\mathcal{G}_{11}s_{11} + \mathcal{A}_1 - \dot{h}_{d1} + \mathcal{B}_1 u_1\right) + e_1\left(\mathcal{G}_{11}s_{11} - \frac{1}{\tau_1}e_1 - \dot{h}_{c1}\right) \\
&\le -\left(k_{11} - \frac{|\mathcal{G}_{11}|}{2}\right)s_{11}^2 - k_{21}s_{21}^2 - \left(\frac{1}{\tau_1} - \frac{|\mathcal{G}_{11}| + 1}{2}\right)e_1^2 + \beta_2 \\
&\le -\alpha V_2 + \beta_2
\end{aligned}$$

$$(.6)$$

where $\beta_2 = \frac{1}{2}\dot{h}_{c1}^2$. For any set $\Omega_{\gamma 1} = \left\{ x_{e1} = [s_{11}, s_{21}, e_1]^T : V_2(x_{e1}) \leq \gamma \right\}$, the function $\dot{V}_2 < 0$ when $\alpha \geq \frac{\beta_2}{\gamma}$. Thus, the control output signal y_1 is asymptotically ISS under fault f_1 and maintains an arbitrarily small tracking error by selecting large k_{11}, k_{21} and $1/\tau_1$. This completes the proof.

Proof of Theorem 3.

For the system stability, choose the Lyapunov function candidate as

$$V_3 = V_1 + \frac{1}{2}e_3^2 \tag{.7}$$

Taking the time derivative of V_3 along the error dynamics (38) and (39) and canceling the integral terms, we obtain

$$
\begin{aligned}
\dot{V}_3 &= s_{11}\left(\mathcal{F}_1 - \dot{y}_1^* + \mathcal{G}_{11}h_{c1} + \mathcal{G}_{12}h_{c2} + \mathcal{H}_1\widehat{f}_2 - \dot{f}_2\right) + s_{12}\left(\mathcal{F}_2 - \dot{y}_2^*\right.\\
&\quad \left. + \mathcal{G}_{22}h_{c2} + \mathcal{H}_2\widehat{f}_2\right) + s_{11}\mathcal{G}_{11}(s_{21} + e_1) + s_{11}\mathcal{G}_{12}(s_{22} + e_2)\\
&\quad + s_{11}\mathcal{H}_1 e_3 + s_{12}\mathcal{G}_{22}(s_{22} + e_2) + s_{12}\mathcal{H}_2 e_3 + s_{21}\left(\mathcal{A}_1 - \dot{h}_{d1}\right.\\
&\quad \left. + \mathcal{B}_1 u_1\right) + s_{22}\left(\mathcal{A}_2 - \dot{h}_{d2} + \mathcal{B}_2 u_2 + \mathcal{C}_2\widehat{f}_2\right) + s_{22}\mathcal{C}_2 e_3\\
&\quad + e_1\left(-\frac{1}{\tau_1}e_1 - \dot{h}_{c1}\right) + e_2\left(-\frac{1}{\tau_2}e_2 - \dot{h}_{c2}\right) + e_3\left(-l_1 e_3 + \dot{f}_2\right)\\[6pt]
&\quad + s_{22}\left(\mathcal{A}_2 + \mathcal{C}_2\widehat{f}_2 + \mathcal{G}_{12}s_{11} + \mathcal{G}_{22}s_{12} - \dot{h}_{d2} + \mathcal{B}_2 u_2\right)\\
&\quad + e_1\left(\mathcal{G}_{11}s_{11} - \frac{1}{\tau_1}e_1 - \dot{h}_{c1}\right) + e_2\left(\mathcal{G}_{12}s_{11} + \mathcal{G}_{22}s_{12} - \frac{1}{\tau_2}e_2 - \dot{h}_{c2}\right)\\
&\quad + e_3\left(\mathcal{H}_1 s_{11} + \mathcal{H}_2 s_{12} + \mathcal{C}_2 s_{22} - l_1 e_3 + \dot{f}_2\right)\\
&= -k_{11}s_{11}^2 - k_{12}s_{12}^2 - k_{21}s_{21}^2 - k_{22}s_{22}^2 - s_{11}\dot{f}_2\\
&\quad + e_1\left(\mathcal{G}_{11}s_{11} - \frac{1}{\tau_1}e_1 - \dot{h}_{c1}\right) + e_2\left(\mathcal{G}_{12}s_{11} + \mathcal{G}_{22}s_{12} - \frac{1}{\tau_2}e_2 - \dot{h}_{c2}\right)\\
&\quad + e_3\left(\mathcal{H}_1 s_{11} + \mathcal{H}_2 s_{12} + \mathcal{C}_2 s_{22} - l_1 e_3 + \dot{f}_2\right)
\end{aligned}
\tag{.8}
$$

With the use of Young's inequality, equation (0.8) is extended as

$$
\begin{aligned}
\dot{V}_3 &\leq -\left(k_{11} - \frac{|\mathcal{G}_{11}| + |\mathcal{G}_{12}| + |\mathcal{H}_1| + 1}{2}\right)s_{11}^2 - \left(k_{12} - \frac{|\mathcal{G}_{22}| + |\mathcal{H}_2|}{2}\right)s_{12}^2\\
&\quad - k_{21}s_{21}^2 - \left(k_{22} - \frac{|\mathcal{C}_2|}{2}\right)s_{22}^2 - \left(\frac{1}{\tau_1} - \frac{|\mathcal{G}_{11}| + 1}{2}\right)e_1^2\\
&\quad - \left(\frac{1}{\tau_2} - \frac{|\mathcal{G}_{12}| + |\mathcal{G}_{22}| + 1}{2}\right)e_2^2 - \left(l_1 - \frac{|\mathcal{H}_1| + |\mathcal{H}_2| + |\mathcal{C}_2| + 1}{2}\right)e_3^2 + \beta_3\\
&\leq -\alpha V_3 + \beta_3,
\end{aligned}
\tag{.9}
$$

where $\beta_3 = \dot{f}_2^2 + \frac{1}{2}\dot{h}_{c1}^2 + \frac{1}{2}\dot{h}_{c2}^2$. Following the proof of Theorem 3.1, the result in (0.9) admits the ISS property of the closed-loop system. Furthermore, the tracking error converges to a sufficiently small neighborhood of the reference when $\dot{f}_2 \to 0 \Rightarrow \beta_3 \to \beta_1$. Thus, the FTC performance is maintained without any degradation, and the proof is completed.

REFERENCES

[1] Rogelj J, den Elzen M, Hoehne N, et al. Paris agreement climate proposals need a boost to keep warming well below 2°C. Nature 2016;534:631–9. http://dx.doi.org/10.1038/nature18307.

[2] Wang Y, Chen KS, Mishler J, et al. A review of polymer electrolyte membrane fuel cells: Technology, applications, and needs on fundamental research. Appl Energy 2011;88(4):981–1007. http://dx.doi.org/10.1016/j.apenergy.2010.09.030.

[3] Duad WRW, Rosli RE, Majlan EH, et al. PEM fuel cell system control: a review. Renew Energy 2017;113:620–38. http://dx.doi.org/10.1016/j.renene.2017.06.027.

[4] Yuan H, Dai H, Wei X, et al. Model-based observers for internal states estimation and control of proton exchange membrane fuel cell system: a review. J Power Sources 2020;468:228376. http://dx.doi.org/10.1016/j.jpowsour.2020.228376.

[5] Danzer MA, Wilgelm J, Aschemann H, et al. Model-based control of cathode pressure and oxygen excess ratio of a PEM fuel cell system. J Power Sources 2008;176(2):515–22. http://dx.doi.org/10.1016/j.jpowsour.2007.08.049.

[6] Gao J, Li M, Hu Y, et al. Challenges and developments of automotive fuel cell hybrid power system and control. Sci China Inf Sci 2019;62(5):051201. http://dx.doi.org/10.1007/s11432-018-9690-y.

[7] Hou J, Yang M, Ke C, et al. Control logics and strategies for air supply in PEM fuel cell engines. Appl Energy 2020;269:115059. http://dx.doi.org/10.1016/j.apenergy.2020.115059.

[8] Al-Durra A, Yurkovich S, Guezennec Y. Study of nonlinear control schemes for an automotive traction PEM fuel cell system. Int J Hydrogen Energy 2010;35:11291–307. http://dx.doi.org/10.1016/j.ijhydene.2010.07.046.

[9] da Fonseca R, Bideaux E, Gerard M, et al. Control of PEMFC system air group using differential faltness approach: validation by a dynamic fuel cell system model. Appl Energy 2014;113:219–29. http://dx.doi.org/10.1016/j.apenergy.2013.07.043.

[10] Ramospaja CA, Giral R, Martinezsalamero L, et al. A PEM fuel-cell model featuring oxygen-excess-ratio estimation and power-electronics interaction. IEEE Trans Ind Electron 2010;57(6):1914–24. http://dx.doi.org/10.1109/TIE.2009.2026363.

[11] Olabi AG, Wilberforce T, Abedlkareem MA. Fuel cell application in the automotive industry and future perspective. Energy 2021;214:118955. http://dx.doi.org/10.1016/j.energy.2020.118955.

[12] Pukrushpan JT, Stefanopoulou A, Peng H. Control of fuel cell power systems: principles, modeling and analysis and feedback design. London: Springer-Verlag; 2004.

[13] Na WK, Gou B. Feedback-linearization-based nonlinear control for PEM fuel cells. IEEE Trans Energy Convers 2008;23(1):179–90. http://dx.doi.org/10.1109/TEC.2007.914160.

[14] Kancsar J, Kozek M, Jakubek S. Flatness-based feedforward control of polymer electrolyte membrane fuel cell gas conditioning system. Int J Hydrogen Energy 2016;41:17526–38. http://dx.doi.org/10.1016/j.ijhydene.2016.06.086.

[15] Chen J, Liu Z, Wang F, et al. Optimal oxygen excess ratio control for PEM fuel cells. IEEE Trans Contr Syst Technol 2009;26(5):1711–21. http://dx.doi.org/10.1109/TCST.2017.2723343.

[16] Kunusch C, Puleston PF, Mayosky MA, et al. Sliding mode strategy for PEM fuel cells stacks brathing control using a super-twisting algorithm. IEEE Trans Contr Syst Technol 2009;17(1):167—74. http://dx.doi.org/10.1109/TCST.2008.922504.

[17] Pilloni A, Psano A, Usai E. Observer-based air excess ratio control of a PEM fuel cell system via high-order sliding mode. IEEE Trans Ind Electron 2015;62(8):5236—46. http://dx.doi.org/10.1109/TIE.2015.2412520.

[18] Matraji I, Ahmed FS, Laghrouche S. Comparison of robust and adaptive second order sliding mode control in PEMFC air-feed systems. Int J Hydrogen Energy 2015;40:9491—504. http://dx.doi.org/10.1016/j.ijhydene.2015.05.090.

[20] Liu J, Gao Y, Su X, et al. Disturbance-observer-based control for air management of PEM fuel cell systems via sliding mode technique. IEEE Trans Contr Syst Technol 2019;27:1129—38. http://dx.doi.org/10.1109/TCST.2018.2802467.

[21] Gruber JK, Doll M, Bordons C. Design and experimental validation of a constrained MPC for the air feed of a fuel cell. Contr Eng Pract 2009;17:874—85. http://dx.doi.org/10.1016/j.conengprac.2009.02.006.

[22] Gruber JK, Bordons C, Oliva A. Nonlinear MPC for the airflow in a PEM fuel cell using a Volterra series model. Contr Eng Pract 2012;20:205—17. http://dx.doi.org/10.1016/j.conengprac.2011.10.014.

[23] Zhang H, An A, Xu T. Nonlinear generalized predictive control for air flow rate regulation in the PEM fuel cell system. Int J Control Autom 2016;9(10):89—100. http://dx.doi.org/10.1016/j.jprocont.2013.01.011.

[24] Hu Y, Chen H, Gong X, et al. Control-oriented modeling and robust nonlinear triple-step controller design for an air-feed system for polymer electrolyte membrane fuel cells. Asian J Contr 2019;21:1811—23. http://dx.doi.org/10.1002/asjc.2146.

[25] Ma Y, Zhang F, Gao J, et al. Oxygen excess ratio control of PEM fuel cells using observer-based nonlinear triple-step controller. Int J Hydrogen Energy 2020;45:29705—17. http://dx.doi.org/10.1016/j.ijhydene.2019.10.089.

[26] Swaroop D, Hedrick JK, Yip PP, et al. Dynamic surface control for a class of nonlinear systems. IEEE Trans Automat Contr 2000;45(10):1893—9. http://dx.doi.org/10.1109/TAC.2000.880994.

[27] Zhang Z, Duan G, Zhou M. An improved adaptive dynamic surface control approach for uncertain nonlinear systems. Int J Adapt Contr Signal Process 2018;32:713—28. http://dx.doi.org/10.1002/acs.2870.

[28] Xu L, Li J, Ouyang M, et al. Active fault tolerance control system of fuel cell hybrid city bus. Int J Hydrogen Energy 2010;35:12510—20. http://dx.doi.org/10.1016/j.ijhydene.2010.08.005.

[29] Lebreton C, Benne M, Damour C, et al. Fault tolerant control strategy applied to PEMFC water management. Int J Hydrogen Energy 2015;40:10636—46. http://dx.doi.org/10.1016/j.ijhydene.2015.06.115.

[30] Wu X, Zhou B. Fault tolerance control for proton exchange membrane fuel cell systems. J Power Sources 2016;324:804—29. http://dx.doi.org/10.1016/j.jpowsour.2016.05.066.

[31] Polverino P, Frisk E, Jung D, et al. Model-based diagnosis through structural analysis and causal computation for automotive polymer electrolyte membrane fuel cell systems. J Power Sources 2017;357:26—40. http://dx.doi.org/10.1016/j.jpowsour.2017.04.089.

[32] Luppi PA, Braccia L, Patrone M, et al. Control allocation based fault-tolerant strategy for a bio-ethanol processor system integrated to a PEM fuel cell. J Process Contr 2019;81:40—53. http://dx.doi.org/10.1016/j.jprocont.2019.05.021.

[33] Yan C, Chen J, Liu H, et al. Model-based fault tolerant control for the thermal management of PEMFC systems. IEEE Trans Ind Electron 2020;67(4):2875—84. http://dx.doi.org/10.1016/j.conengprac.2016.11.017.

[34] Yang D, Wang Y, Chen Z. Robust fault diagnosis and fault tolerant control for PEMFC system based on an augmented LPV observer. Int J Hydrogen Energy 2020;45:13508—22. http://dx.doi.org/10.1016/j.ijhydene.2020.03.063.

[35] Lan J, Patton RJ. A new strategy for integration of fault estimation within fault-tolerant control. Automatica 2016;69:48—59. http://dx.doi.org/10.1016/j.automatica.2016.02.014.

[36] Gravdahl JT, Egeland O. Compressor surge and rotating stall: modeling and control. New York:Springer Science & Business Media; 2012.

[37] Larminie J, Dicks A. Fuel cell systems explained. London: Wiley; 2003.

[38] Heywood JB. Internal combustion engine fundamentals. New York: McGraw-Hill Education; 2018.

[39] Zhang H, Wang Y, Wang D, et al. Adaptive robust control of oxygen excess ratio for PEMFC system based on type-2 fuzzy logic system. Inf Sci 2020;511:1—17. http://dx.doi.org/10.1016/j.ins.2019.08.005.

[40] Wang Y, Yu S, Yuan J, et al. Fault-tolerant control of electric ground vehicles using a triple-step nonlinear approach. IEEE-ASME T Mech 2018;23(4):1775—86. http://dx.doi.org/10.1109/TMECH.2018.2837128.

[41] Wang Y, Kim Y. Real-time control for air excess ratio of a PEM fuel cell system. IEEE-ASME T Mech 2014;3(19):852—61. http://dx.doi.org/10.1016/j.ijhydene.2014.05.153.

[42] Sankar K, Jana AK. Nonlinear multivariable sliding mode control of a reversible PEM fuel cell integrated system. Energy Convers Manag 2018;171:541—65. http://dx.doi.org/10.1016/j.enconman.2018.05.079.

[43] Petrone R, Zheng Z, Hissel D, et al. A review on model-based diagnosis methodologies for PEMFCs. Int J Hydrogen Energy 2013;38:7077—91. http://dx.doi.org/10.1016/j.ijhydene.2013.03.106.

[44] Collong S, Kouta R. Fault tree analysis of proton exchange membrane fuel cell system safety. Int J Hydrogen Energy 2015;40:8248—60. http://dx.doi.org/10.1016/j.ijhydene.2015.04.101.